Petroleum Science 23 (2026) 3777–3804

Contents lists available at ScienceDirect

Petroleum Science

journal homepage: www.keaipublishing.com/en/journals/petroleum-science

Review Paper

A multiple review on identification and fine evaluation of shale pores: Prospects and challenges

Qi-Yang Gou [a,b], Shang Xu [a,*], Fang Hao [a,**], Ke-Yu Liu [a], Zhang-Xing Chen [b,c]

[a] State Key Laboratory of Deep Oil and Gas, China University of Petroleum (East China), Qingdao, 266580, Shandong, China
[b] Department of Chemical and Petroleum Engineering, Schulich School of Engineering, University of Calgary, Calgary, Alberta, T2N 1N4, Canada
[c] Eastern Institute for Advanced Study, Ningbo, 315000, Zhejiang, China

ARTICLE INFO

Article history:
Received 3 June 2025
Received in revised form
11 November 2025
Accepted 6 May 2026
Available online 12 May 2026

Edited by Xiu-Fang Hu

Keywords:
Shale pore evaluation
Sample preparation
Experimental parameters
Data processing challenges
Standardized protocols

ABSTRACT

Accurate evaluation of pore systems in shale reservoirs is critical for understanding fluid flow, gas storage capacity, and overall reservoir performance. Extensive research has been conducted on the micro- and nano-pore structure of shale reservoirs using various experimental methods and shale samples. However, discrepancies in sample preparation standards and experimental parameters—such as observation techniques and data interpretation—raise concerns about the reliability and comparability of these results across different shale reservoirs. This review systematically evaluates the current methods for characterizing shale pore systems, with particular emphasis on commonly used techniques such as scanning electron microscopy (SEM), gas adsorption, and CT scanning. Key challenges related to sample preparation (e.g., sample size) and experimental conditions (e.g., voltage and current) are discussed, as these factors can introduce significant inaccuracies into pore structure characterization, even for well-established methods. Additionally, we examine the difficulties in integrating these methods to achieve a comprehensive understanding of shale pore parameters, including the quantification of organic and inorganic porosity, full-scale pore size distribution, and pore connectivity. Addressing these challenges requires the establishment of standardized processing workflows to enhance the comparability of results and minimize experimental errors. We also highlight often-overlooked issues, such as the potential discrepancy between pore structures observed under laboratory conditions and those at in-situ depths. The review concludes with recommendations for future research, including the development of advanced experimental techniques and more efficient data processing strategies to improve pore characterization in shale reservoirs. This review provides a new perspective for future research and addresses a critical gap in understanding the impact of experimental conditions on pore structure characterization outcomes.

1. Introduction

The global economic expansion and the resulting surge in energy demand have exacerbated the conflict between supply and demand. Unconventional energy resources, such as shale oil and shale gas, are crucial alternatives to conventional sources and have garnered significant attention. Over the past decade, the development and utilization of hydrocarbons from shale systems have expanded considerably. Shale gas resources, in particular, hold significant promise, with technically recoverable resources estimated at 2.1×10^5 bcm (Zou et al., 2023). Researchers worldwide generally agree that accelerating the utilization of shale gas is a key strategy to address the energy gap (Arif et al., 2021; Bera and Shah, 2021; Cai et al., 2024).

Shales serve as self-generating and self-storing reservoir systems (Hao and Zou, 2013; Katz and Arango, 2018). Hydrocarbons are primarily stored in ultra-fine pores and micro-fractures, existing in both free and adsorbed states (Slatt and O'Brien, 2011; Loucks et al., 2012; Löhr et al., 2015; Arif et al., 2021). The pore structure influences shale gas occurrence, with free gas

* Corresponding author.
** Corresponding author.
E-mail addresses: xushang@upc.edu.com (S. Xu), haofang@cug.edu.cn (F. Hao).
Peer review under the responsibility of China University of Petroleum (Beijing).

https://doi.org/10.1016/j.petsci.2026.05.003

content directly determining the initial production rates and estimated ultimate recovery of gas wells (Clarkson et al., 2013, 2016; Milliken et al., 2013; Feng et al., 2018; Gou and Xu, 2019; Wu et al., 2020a). While hydraulic fracturing is considered essential for commercial shale gas production, the microscopic pore structure also plays a critical role in the flow of gas from matrix pores to hydraulic fractures (Clarkson et al., 2016; Gou and Xu, 2019). Pore structure is a key parameter in controlling shale reservoir quality, gas molecule migration, and accumulation (Bera and Shah, 2021; Gou et al., 2023). Understanding pore network characteristics is crucial for accurately predicting hydrocarbon production and optimizing extraction processes (Anovitz and Cole, 2015; Lai et al., 2018).

Over the past decade, substantial research has been dedicated to the description and quantification of pore space in shale reservoirs (Loucks et al., 2009, 2012; Milliken and Reed, 2010; Curtis et al., 2012a, 2012b; Ruppert et al., 2013; Tian et al., 2013; Saif et al., 2017; Gou et al., 2019, 2021; Xu et al., 2020a, 2020b; Blach et al., 2021). The influence of various factors, including organic richness, thermal maturity, organic type, mineral composition, and preservation conditions on pore structure, has also been reviewed (Anovitz and Cole, 2015; Ougier-Simonin et al., 2016; Katz and Arango, 2018; Gao et al., 2020; Afagwu et al., 2022; Jiang et al., 2023; Wang and Cheng, 2023; Zhao et al., 2023a). However, existing studies often focus on method descriptions, with limited attention to the critical analysis of preprocessing-induced errors, which can significantly affect pore structure evaluations. This gap highlights the novelty and necessity of the present work, which aims to provide a comprehensive, systematic approach to pore structure characterization that considers the impacts of sample preparation and data post-processing.

In the following sections, we summarize various approaches used for pore structure recognition. While some of these methods have been previously introduced, newer technologies (e.g., scattering methods) are also discussed. We provide a thorough overview of pore classification based on location, availability, and size. The challenges regarding sample preparation and data post-processing for common experimental methods (e.g., gas adsorption and scanning electron microscopy) are analyzed, and several recommendations are proposed. The prospects and challenges of fine characterization of shale reservoirs are also explored. In the concluding section, we outline potential research focuses and development trends. This review aims to foster the development of standardized data analysis and processing methods, facilitating more accurate comparisons across studies.

2. Various methods for the investigation of shale reservoirs

In shale reservoirs, key microstructural features, such as pores, fractures, organic matter (OM), and matrix minerals, are of particular importance (Fig. 1) (Anovitz and Cole, 2015; Ma et al., 2017; Kwiecińska et al., 2019). These features, however, exhibit significant heterogeneity across various scales (Katz and Arango, 2018; Arif et al., 2021; Chandra and Vishal, 2021). Over the past decade, a range of visualization and quantitative techniques have been employed to precisely characterize and quantify these properties (Fig. 1).

2.1. Utilization of imaging methods

2.1.1. 2D imaging methods

The 2D visualization of pores in shale samples relies on a variety of imaging techniques, including transmission electron microscopy (TEM) (Chalmers et al., 2012; Bernard et al., 2013), helium ion microscopy (HIM) (Sun et al., 2020a; Chandra and Vishal, 2021), field emission scanning electron microscopy (FE-SEM) (Bernard et al., 2012; Curtis et al., 2012a, 2012b; Loucks et al., 2012; Saif et al., 2017; Gou et al., 2019), and optical microscopy (Bultreys et al., 2016; Chandra et al., 2020). These techniques enable direct observation of pore geometry, distribution, type, and size (Table 1 and Fig. 1) (Milner et al., 2010; Slatt and O'Brien, 2011; Klaver et al., 2012; Milliken et al., 2013; Löhr et al., 2015; Blach et al., 2021; Gou et al., 2021; Zhu et al., 2021; Liu et al., 2022). However, the limited observation area and insufficient representativeness of high-resolution images produced by these methods should be noted (Klaver et al., 2012; Sun et al., 2020a; Wang et al., 2024). For FE-SEM, the use of ion polishing to produce a flat surface remains controversial, and the instrument's limitations constrain the smallest recognizable pore size (Table 1). Parameter settings also influence image quality (see section 4.4).

2.1.2. 3D imaging methods

Recently, 3D imaging techniques have enabled the calculation of key geometric attributes such as porosity, pore volume, pore size, and connectivity (Table 1 and Fig. 1) (Lai et al., 2018; Gou et al., 2019, 2021; Wu et al., 2019, 2020b; Arif et al., 2021; Saraf and Bera, 2021; Zhu et al., 2021). These advancements provide a deeper understanding of the storage and migration mechanisms of oil and gas molecules within reservoirs (Ma et al., 2017; Arif et al., 2021; Saraf and Bera, 2021). X-ray nano- and micro-CT are commonly employed to examine the spatial connectivity and distribution of pores and micro-fractures (Gou et al., 2019; Sun et al., 2020b; Zhao et al., 2020; Zou and Sun, 2020; Arif et al., 2021). The spatial resolution of nano-CT is approximately 65 nm, while micro-CT has a resolution of about 700 nm (Table 1) (Gou et al., 2019; Chandra and Vishal, 2021). Nano-CT scanning requires small samples, typically cylindrical with a diameter of 65 μm (Wang et al., 2016; Wu et al., 2019), which complicates sample preparation (Table 1). Although micro-CT has less stringent sample size requirements, to achieve higher resolution, very small samples are typically used, which creates a challenge in balancing sample representativeness with resolution (Gou et al., 2019; Arif et al., 2021). Furthermore, selecting appropriate algorithms for pore and micro-fracture extraction, along with potential human biases, poses challenges that need to be addressed in future research (Fitschen et al., 2017; Fan et al., 2022). Focused ion beam scanning electron microscopy (FIB-SEM) generates a series of sequential SEM images through serial sectioning, facilitating 3D characterization of nanopores (Curtis et al., 2012b; Anovitz and Cole, 2015; Yang et al., 2025). It achieves a penetration depth of approximately 3–5 nm; however, the extremely small sample area necessitates consideration of scale and potential sample bias (Silin and Kneafsey, 2012; Anovitz and Cole, 2015). Like CT scanning, FIB-SEM has high operational costs, which limit the number of samples that can be analyzed (Table 1).

2.2. Applications of fluid invasion methods

Fluid injection techniques, including low-pressure gas adsorption (using N_2, CO_2, and Ar), mercury injection capillary pressure (MICP), and helium (He) porosimetry (Fig. 1), are primarily employed to evaluate pore volume and pore size distribution (Giesche, 2006; Clarkson et al., 2013, 2016; Mastalerz et al., 2013; Schmitt et al., 2013; Tinni et al., 2014a; Anovitz and Cole, 2015; Sun et al., 2020a; Iqbal et al., 2021).

2.2.1. Gas adsorption

The range of pore sizes probed by gas adsorption techniques depends on the properties of the gas used. The low-pressure N_2 gas adsorption method, conducted at a temperature of 77 K, is most

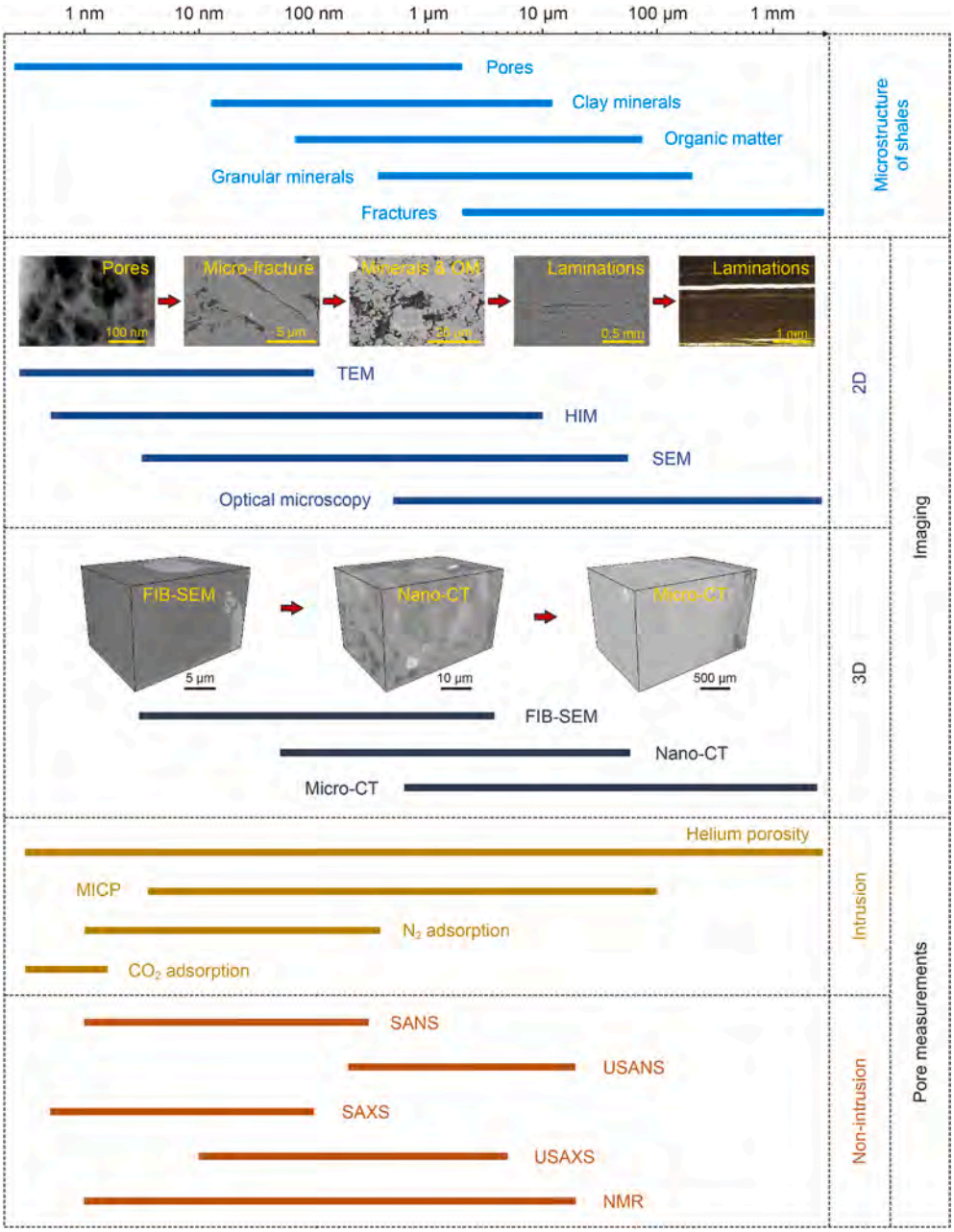

Fig. 1. Multi-scale techniques used to study shale microstructural properties, modified from Ma et al. (2017), Sun et al. (2020a), and Arif et al. (2021).

suitable for materials with pores ranging from 2 nm to 300 nm (Table 1 and Fig. 1), such as those found in shale and coal (Anovitz and Cole, 2015; Liu and Ostadhassan, 2019; Zhou et al., 2024a). The quadrupole moment of the nitrogen molecule interacts with surface functional groups during the test, affecting the orientation of the surface nitrogen molecules and the filling of micropores (<2 nm) (Jiang et al., 2023; Zhou et al., 2024a). As such, it is not typically used for evaluating micropores. Argon, with its advantages for micropore analysis, is limited in accessing pores smaller than 0.45 nm due to its low testing temperature (87.3 K) and slow kinetic activity (Thommes et al., 2015). In contrast, CO_2 adsorption, with its smaller molecular diameter (0.33 nm) and higher test temperature (273 K), facilitates access to ultra-micropores (Chalmers et al., 2012; Mastalerz et al., 2013), making it a common method for micropore analysis and complementary to N_2 adsorption (Table 1) (Bertier et al., 2016; Sun et al., 2020b). Nevertheless, the impact of particle size and analysis models on experimental results, especially with crushed shale samples, remains an ongoing research topic (see sections 4.1 and 4.2).

2.2.2. Mercury injection capillary pressure

The MICP technique is a widely used method for investigating pore-throat distributions in porous shale, ranging from the micro-scale (up to ~350 μm) to the nano-scale (Table 1 and Fig. 1) (Giesche, 2006; Sun et al., 2020a, 2020b; Yang et al., 2025). The mercury intrusion pressure is inversely proportional to pore size, with pores as small as 3 nm being detectable at the maximum pressure of 60,000 psi (414 MPa). However, it is important to note that artificial pores and micro-fractures may form during the high-pressure mercury injection process, which can affect pore

Table 1
Applicability, advantages, and disadvantages of common methods used for evaluating shale pore structure.

Classification of methods		Common types of samples used	Measurable range	Measurable parameters	Key advantages	Main limitations
Imaging methods	TEM	Thin wafer-like sample (up to ~100 nm thick)	>~0.2 nm	Pore morphology, particle size distribution	High resolution for nanoscale structures	Sample thickness limitation, minimal scanning area, and sample preparation complexity
	HIM	Block samples	>~0.5 nm	Pore morphology, particle size distribution	High-resolution surface imaging, sensitivity to nanostructures	Limited field of view, sample preparation complexity
	FE-SEM	Block samples	>~2 nm	2D pore type, pore quantity, pore size distribution, surface morphology	High resolution, surface analysis	Limited depth of field, potential for charging effect, and expensive
	FIB-SEM	Block samples, cross-sections	>~3–5 nm	Pore morphology, 3D pore structure	High precision in 3D pore structure analysis, sample sectioning	Time-consuming, complex sample preparation, and minimal scanning area
	Nano-CT	A small cylinder with a diameter of 65 μm	>~65 nm	Pore size distribution, pore connectivity, 3D pore structure	Non-destructive, 3D imaging of internal structure	Limited resolution for very small pores, expensive equipment, and minimal scanning area
	Micro-CT	Small and large block samples	>~700 nm	3D pore and micro-fracture structure	Non-destructive, wide application, 3D imaging, quick results	Limited resolution for small pores, and minimal scanning area
Fluid invasion methods	He-porosity	Plunger samples, block samples, powdered samples	>~0.2 nm	Total porosity	Simple, fast, cost-effective, precise porosity measurement	Cannot characterize pore size distribution
	CO_2 adsorption	Powdered samples	<2 nm	Surface area, micropore volume, pore size distribution	Excellent for characterizing micropores	Limited to micropores
	N_2 adsorption	Powdered samples	2–300 nm	Surface area, mesopore and some macropore volume, pore size distribution	Widely used, high reproducibility, detailed pore characterization	Primarily for mesopores and some macropores, not suitable for very small pores and large pores
	MICP	Plunger samples, block samples	~3 nm–350 μm	Pore size distribution, porosity, and capillary pressure	Accurate pore size distribution, effective for large pores	Requires sample pre-treatment, assumes cylindrical pore shapes, and does not resolve small pores well
Non-fluid invasion methods	(U)SANS	Thin wafer-like samples, small particle samples	~1 nm to 20 μm	Pore structure, connectivity, nanoscale porosity	Can measure nanoscale pores, non-destructively	Requires advanced data analysis, limited by sample size and preparation
	(U)SAXS	Thin wafer-like samples, small particle samples	~0.5 nm to 50 μm	Pore structure, connectivity, nanoscale porosity	Non-destructive, multi-scale measurements, sensitive to small pores	High cost, specialized equipment, and data interpretation required
	NMR	Plunger samples	>~1 nm	Porosity, fluid distribution, pore connectivity	Non-destructive, excellent for porosity and fluid distribution measurements	Requires sample saturation, complex data interpretation, and sensitivity to magnetic field inhomogeneities

structure parameters (Wang et al., 2019a; Jiang et al., 2023). For example, Wang et al. (2015a) observed that shale samples may deform when the mercury intrusion pressure exceeds 25 MPa, and pressures must reach 110 MPa before significant changes in shale pore volume occur (Wang et al., 2019b). Furthermore, shale storage space typically consists of both pores and throats (Lai et al., 2018). The throat diameter is generally smaller than that of the pore, which requires higher pressure to overcome the capillary forces of the throat during mercury intrusion. Consequently, high-pressure mercury injection tests may overestimate the pore volume of smaller pores (Katz and Thompson, 1986; Torabi et al., 2013; Jiao et al., 2020). Therefore, this technique is most commonly used to characterize pore structures with diameters >50 nm, or even >100 nm (Table 1), in sediments (Wang et al., 2015a; Iqbal et al., 2021).

2.2.3. He-porosimetry

He-porosimetry is a well-established, comprehensive, and widely used method for characterizing the effective storage capacity of shale reservoirs (Kuila et al., 2014; Yang et al., 2015; Zhou et al., 2021). However, a few caveats should be considered. One issue is the testing error between crushed and core samples; the porosity of crushed shale samples may be 0.1% to 0.2% higher than that of core samples (Luffel and Guidry, 1992; Anovitz and Cole, 2015; Yang et al., 2015; Zhou et al., 2021). Another limitation is that He-porosimetry cannot provide detailed information about the geometry, location, or size of individual pores (Table 1) (Zhang et al., 2020; Zhu et al., 2021).

2.3. Employment of non-fluid invasion methods

2.3.1. Small-angle scattering

Ultra-small and small-angle scattering ((U)SAS) techniques offer relatively new tools for characterizing both connected and closed pores (Clarkson et al., 2013; Ruppert et al., 2013). These techniques employ neutron or X-ray beams to penetrate rock and measure the intensity of scattered signals within a specific scattering angle, providing valuable information about the shale pore

structure (Radlinski et al., 2004; Lee et al., 2014). Small-angle neutron scattering (SANS) is generally more commonly used than small-angle X-ray scattering (SAXS) due to the superior penetration capabilities of neutrons (Sun et al., 2020a). (U)SAS technology enables the characterization of pore structures across a wide range of scales, from sub-nanometers to tens of micrometers (e.g., from 0.5 nm to 20 μm, Table 1 and Fig. 1) (Anovitz and Cole, 2015). Moreover, there are no strict restrictions on the size or form of the samples, which can be in powder form (e.g., with a particle size of 80 mesh) or in wafer form (typically with a thickness of less than 1 mm). Thin sheet samples can be directly clamped or affixed to the sample holder, whereas particle samples must be placed in cuvettes made from materials with high neutron transmittance (e.g., quartz, sapphire). When selecting the sample thickness, the influence of the neutron wavelength should be considered. Longer wavelengths decrease neutron transmittance and increase the likelihood of multiple scattering, thereby reducing data quality (Ruppert et al., 2013; Anovitz and Cole, 2015). To minimize multiple scattering caused by gaps between particles, it is generally recommended to use samples with a particle size of ~0.5 mm (Sun et al., 2020a, 2020b). Currently, a variety of interpretation models have been proposed to convert SAS results from relatively simple materials into pore-size distributions. These include the smooth surface approach (Anovitz et al., 2013), the polydisperse hard sphere model (Radlinski, 2006), regularization or maximum smoothness (Svergun, 1991), and total non-negative least squares (Ilavsky and Jemian, 2009). However, for highly inhomogeneous shale reservoirs with complex pore and mineral compositions, the relationship between scattering intensity and pore size remains unclear (Anovitz et al., 2013). There is no satisfactory explanation for the scattering intensity and data modeling in the current literature (Jiang et al., 2023). Furthermore, some studies do not specify the neutron wavelength (Anovitz and Cole, 2015; Sun et al., 2020a). In summary, SAS technology is still in its early stages in the field of pore structure characterization of shale reservoirs, and further modeling and investigation are required.

2.3.2. Nuclear magnetic resonance

Nuclear magnetic resonance (NMR) is an emerging non-destructive technique for detecting the pore structure of rock samples. It is based on the polarization of hydrogen nuclei in materials such as water and hydrocarbon fluids under the influence of a magnetic field, which generates a magnetic vector phenomenon (Zhang et al., 2018a; Bai et al., 2023). The signal intensity decays over time (i.e., relaxation time T_2) is obtained, reflecting the pore structure and fluid distribution characteristics within the reservoir (Table 1) (Yao and Liu, 2018). During the NMR detection process, shale samples typically need to be saturated with fluid to fill the pores, which ensures effective reflection of the internal pore space. This means that the pores detected by NMR are primarily connected pores (Tinni et al., 2014b; Jiang et al., 2023). The selection of probe reagents is also a critical step in NMR testing, with water or oil (including alkanes, kerosene, etc.) commonly used as probe reagents. However, the hydration reaction between water and clay minerals in shale can significantly affect the test results (Sulucarnain et al., 2012; Zhang et al., 2018a; Jiang et al., 2023). The presence of paramagnetic minerals such as pyrite and siderite in shale can shorten the relaxation time, thereby impacting the interpretation of the pore structure. Moreover, crucial parameters like pore size conversion, surface relaxation rate, and shape factor remain highly subjective and lack standardization (Table 1) (Song and Kausik, 2019; Bai et al., 2023). Consequently, NMR is capable of indicating the trend of pore size distribution but not the absolute pore volume.

As mentioned above, using these technical methods in isolation has several obvious limitations. Therefore, combining different characterization methods is necessary to gain a more comprehensive and accurate understanding of pore and fracture structures in shale reservoirs across multiple scales (see section 5.2).

3. Classification of multi-scale pore systems

The primary states of stored shale gas are adsorbed and free, with these gases being widely distributed across pores and microfractures of varying scales within shale reservoirs (Hao and Zou, 2013; Hao et al., 2013; Arif et al., 2021). The type and size of these pores govern the flow, migration, storage, and occurrence mechanisms of oil and gas within geological formations (Katz and Arango, 2018; Bera and Shah, 2021). Evaluating pore types and sizes according to appropriate parameters or standards is essential for accurately characterizing the pore structure of shale.

3.1. Classification by pore development location

Researchers studying complex heterogeneous shale have expanded our understanding of pores based on their relationship to particles (e.g., Kwon et al., 2004; Curtis, 2010; Slatt and O'Brien, 2011; Loucks et al., 2012; Milliken et al., 2013; Yu, 2013). Pore types, ranging from interparticle (interP) and intraparticle (intraP) mineral pores to organic matter (OM) pores and fracture pores, can be hierarchically subdivided (Fig. 2(a)). InterP pores mainly occur between particles or as intercrystalline pores, while intraP pores typically develop within carbonate minerals but can also be found in pyrite, phyllosilicate frameworks, and fossil bodies (Loucks et al., 2012; Katz and Arango, 2018). OM pores, a specific type of intraP pore, are found within organic matter and are closely correlated with the type of organic matter and the thermal maturity of the rocks (Mastalerz et al., 2013; Milliken et al., 2013; Löhr et al., 2015; İnan et al., 2018). Fracture-related pores, not controlled by individual mineral particles, significantly influence hydrocarbon storage, transport, and production (Gale et al., 2007; Slatt and O'Brien, 2011; Loucks et al., 2012; Yang et al., 2021). Additionally, due to the confining effect of particles, certain pore clusters become isolated, leading to the development of another pore classification scheme. Specifically, pores are categorized as closed, open, or blind based on their connectivity to external fluids (Fig. 2(b)). Open pores have continuous channels that connect to external materials, whereas blind pores are only open at one end (Rouquerol et al., 1994; Nishiyama and Yokoyama, 2017).

3.2. Classification by pore size

An additional pore classification, based on pore size, is widely discussed in the literature (Fig. 3). The most common classification divides shale pores into micropores (<2 nm), mesopores (2–50 nm), and macropores (>50 nm) (Rouquerol et al., 1994). Other classification schemes for shale pores also exist (Zou et al., 2011; Loucks et al., 2012; Zhu et al., 2016), but they often fail to effectively distinguish between matrix-related pores and fracture pores. Therefore, a new classification scheme, which considers the differences in pore and fracture sizes, has been proposed (scheme 3 in Fig. 3). This scheme, based on the work of Rouquerol et al. (1994), extracts micro-fractures and clarifies the differences in storage capacity and permeability between pores and micro-fractures (Gou et al., 2019). It is important to note that the pore size classification schemes mentioned above are primarily applied to shale gas reservoirs and may be less applicable to shale oil reservoirs due to significant differences in the sizes of oil and gas molecules (Jin et al., 2021). Despite the lack of an effective

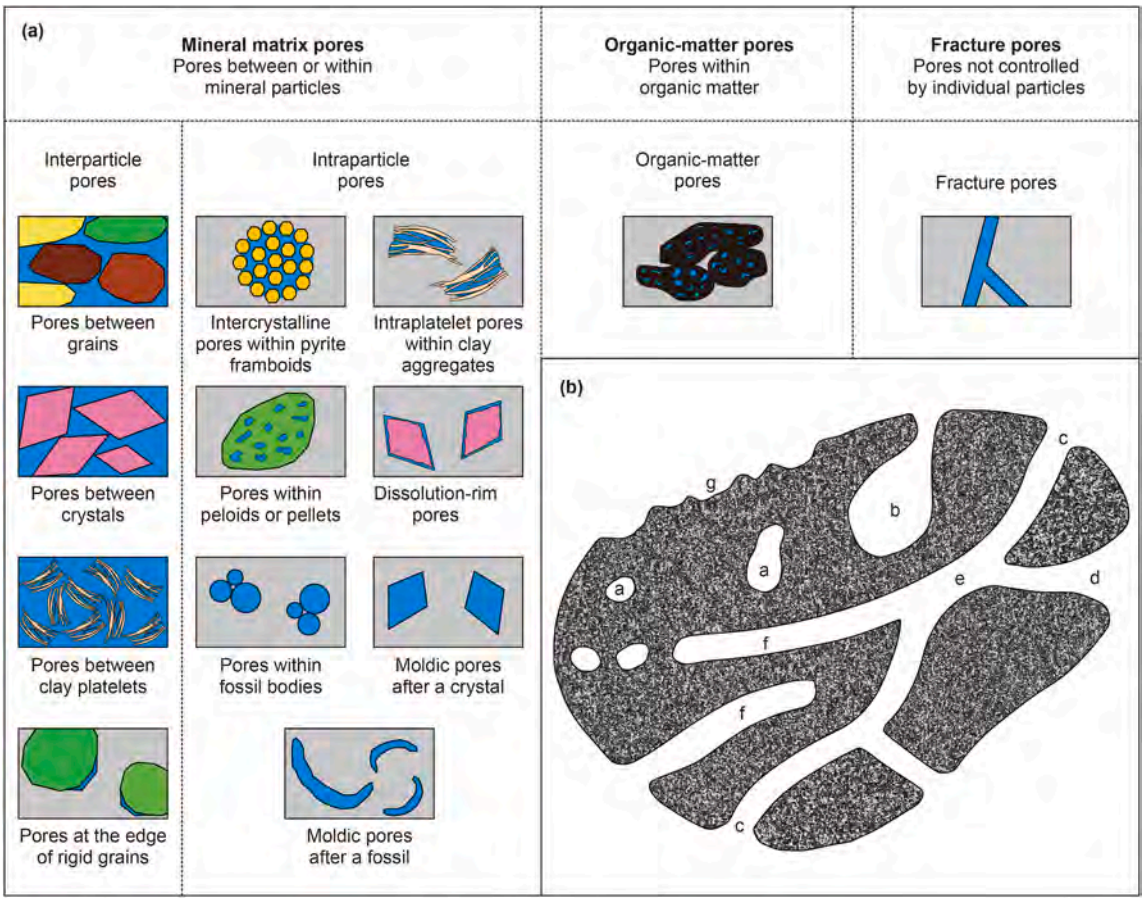

Fig. 2. Spectrum classification for shale storage space, **(a)** proposed on the basis of relationships between pores and mineral particles, pores are represented by blue, modified from Loucks et al. (2012); **(b)** proposed on the basis of the availability of pores to external fluid, a: closed pores; b and f: blind pores; c, d and e: through pores; g: roughness of the external surface; modified from Rouquerol et al. (1994).

classification scheme, most scholars continue to rely on these potentially unsuitable methods (Han et al., 2019; Lei et al., 2021; Liu et al., 2023). Recently, Lu et al. (2018, 2022) proposed a new classification for shale oil reservoirs, categorizing pores into micropores, small pores, mesopores, and macropores based on the inflection points of mercury injection curves and fractal features. However, this scheme has shown significantly different results when applied to various regions and shale formations (schemes 5–8 in Fig. 3) (Lu et al., 2022; Zhao et al., 2022). In response, Gou et al. (2023) combined low-pressure gas adsorption and multiple isothermal stage pyrolysis to propose a new classification scheme, categorizing pores into adsorption pores (<20 nm), restricted pores (20–100 nm), and movable pores (>100 nm). This scheme represents a significant advancement in linking shale oil occurrence and mobility characteristics with pore size and may guide future research.

3.3. Future classification schemes

While the pore classification schemes outlined above have significantly advanced our understanding of shale reservoirs, they have limitations, particularly when applied across diverse geological contexts and fluid types. One key limitation is that many of these schemes focus primarily on the inherent parameters of the pores themselves, failing to incorporate critical petrophysical properties, such as permeability and wettability, which are essential for understanding fluid flow behavior (Loucks et al., 2012; Cai et al., 2024; Wu et al., 2024). For instance, large pores in the matrix may not significantly contribute to permeability if they are poorly connected, while smaller pores in fractures can dominate fluid flow despite their smaller size (Bultreys et al., 2016). Consequently, while pore size-based classification schemes work well for oil and gas storage, their applicability to fluid migration mechanisms may be limited (Jin et al., 2021; Yang et al., 2021).

Shales vary in mineral composition, organic matter content, and thermal maturity, all of which influence pore type, structure, and connectivity (Gao et al., 2020; Wu et al., 2020a; Xu et al., 2024, 2025). Pore type—whether organic or inorganic pores—also strongly influences fluid behavior (Wu et al., 2024). In shale gas reservoirs with high thermal maturity, classifications that emphasize pore locations are commonly used, as these are crucial for understanding pore origin and preservation conditions (Loucks et al., 2009; Ma et al., 2016; Chen et al., 2019; Wu et al., 2020a). In contrast, for shale oil reservoirs with lower thermal maturity, schemes that link pore size with oil mobility, such as those proposed by Gou et al. (2023), may provide more relevant insights. Region-specific adaptations are essential for effective pore classification. In conclusion, while current pore classification schemes contribute to advancing our understanding of shale reservoirs, they still face challenges related to geological and fluid variability across different formations. To enhance the accuracy of these classifications, future research should continue refining these schemes, incorporate additional petrophysical properties such as

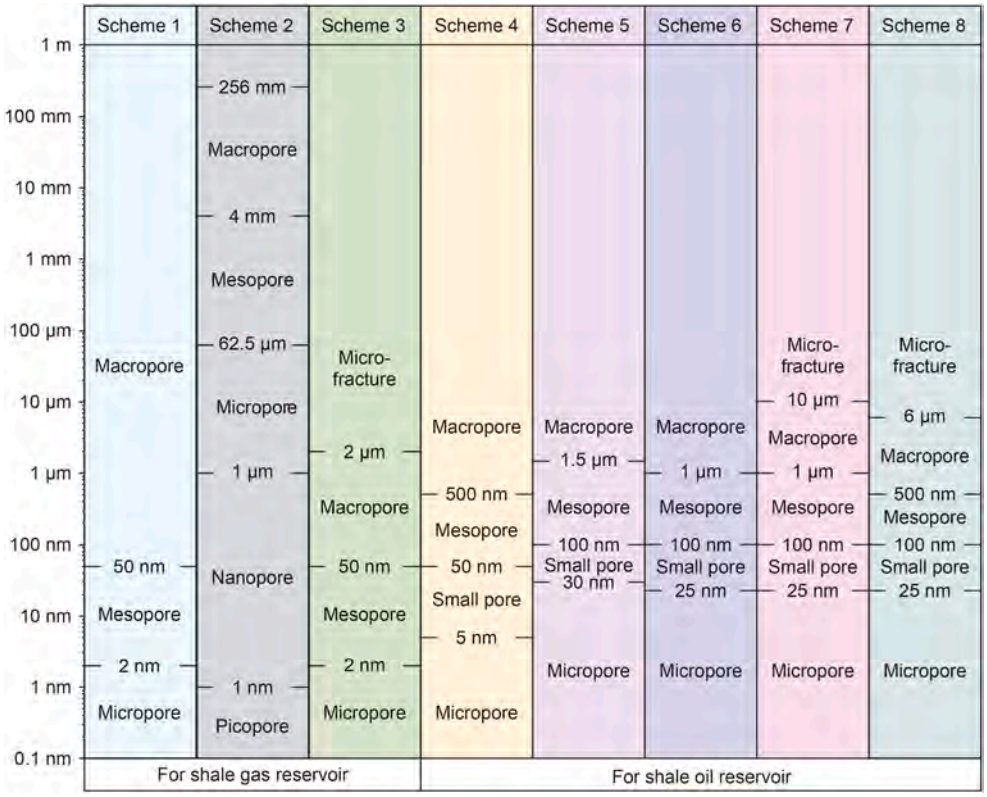

Fig. 3. Spectrum of shale pore types based on pore size. Schemes 1 to 3 primarily focus on the classification of shale gas reservoirs. Scheme 1 is adapted from Rouquerol et al. (1994), scheme 2 is adapted from Loucks et al. (2012), and scheme 3 is adapted from Gou et al. (2019). Schemes 4 to 8 present the results of shale oil reservoir delineation based on mercury injection curves, adapted from Lu et al. (2022).

permeability and wettability, and offer guidance on selecting the most appropriate classification method depending on the specific research objectives (e.g., shale gas vs. shale oil).

4. Key analysis on preprocessing for pore identification

As mentioned earlier, there are numerous methods for characterizing shale reservoirs (Fig. 1). Particularly for experiments such as scanning electron microscopy (SEM) and gas adsorption, they are currently the most widely used and relatively mature technologies (Anovitz and Cole, 2015; Katz and Arango, 2018; Jiang et al., 2023; Zhao et al., 2023a). However, it must be emphasized that although these methods are mature and have been widely applied, they do have limitations, especially in sample preparation and data interpretation (Hazra et al., 2018; Liu et al., 2021). For instance, factors such as sample size, preparation procedures, and experimental conditions (e.g., voltage and current settings) can introduce significant errors, which are often overlooked in routine applications (Zhao et al., 2019; He et al., 2021). Given that these methods have always played a central role in shale research, it is necessary to conduct more in-depth studies on the challenges in these preprocessing aspects before moving on to emerging technologies. Only by improving these traditional methods can we ensure reliable results, which will serve as a solid foundation for integrating new methods and ultimately contribute to a more accurate and comprehensive understanding of the characteristics of shale reservoirs.

4.1. Preparation of sample size for gas adsorption

Low-pressure gas adsorption is a critical technique for quantifying the specific surface area, pore volume, and pore size distribution of nanopores with diameters typically less than 300 nm (Table 1) (Clarkson et al., 2013; Mastalerz et al., 2013, 2017; Bertier et al., 2016). In practice, samples are often crushed prior to measurement, as the experimental results can show a significant correlation with the particle size of the sample (Tinni et al., 2014a; Wei et al., 2016; He et al., 2021). However, no standardized procedure has been universally accepted by researchers to date (Table 2). For shale samples, a size fraction smaller than 20 mesh (i.e., <0.85 mm diameter) is generally recommended (Chen et al., 2015). Han et al. (2016) observed that as particle size decreased from 5 mesh to 130 mesh, the N_2 adsorption capacity increased, with no significant change occurring between the 130 mesh and 250 mesh ranges (Fig. 4). Similar trends were noted in the hysteresis loops, isotherm shape, pore volume, and specific surface area (Figs. 4 and 5). The authors suggest that this phenomenon may be explained as follows: below 130 mesh, finer particle sizes increase the exposure of pores and micro-fractures, thereby enhancing the pore space. Although the authors do not provide additional explanations for this observation, it can be inferred that the maximum pore parameters observed at 130 mesh may also result from additional grinding during sample preparation, which could potentially generate new micro-fractures. Other commonly used analytical size fractions include, but are not limited to, 60–80 mesh (Li et al., 2019; He et al., 2021), 60–140 mesh (Wei et al., 2016), >150 mesh (Hazra et al., 2018), 100–200 mesh (Zhang et al., 2018b), and 200 mesh (Mastalerz et al., 2017) (Table 2). Comparing experimental data from different sources can be challenging due to the variation in grain sizes used in the literature (Ross and Bustin, 2009; Clarkson et al., 2013; Kuila and Prasad, 2013; Tian et al., 2013; Sun et al., 2016; Hazra et al., 2018).

Table 2
Summary of sample particle sizes used in recent years for low-pressure N_2 and CO_2 gas adsorption techniques.

Shale name	Location	R_o, %	Used particle size, mesh	Recommended particle size, mesh	Source
New Albany	Illinois Basin, USA	0.35–1.41	4, 20, 60	<20	Chen et al. (2015)
Longmaxi	Sichuan Basin, China	~1.59	5, 20, 40, 60, 100, 130, 150, 200, 250	130	Han et al. (2016)
Wufeng-Longmaxi	Upper Yangtze, China	~2.0	<60, 60–80, 80–100, 100–120, 120–140, 140–200, >200	60–140	Wei et al. (2016)
New Albany	Illinois Basin, USA	~0.57 and ~1.3	Chunks (~7 mm), 4, 7, 18, 30, 60, 200, 230	200	Mastalerz et al. (2017)
Rajmahal and Barakar	Birbhum Coal Basin and West Bokaro Basin, India	~2.25 and ~0.95	18–35, 35–70, 70–200, 200–270	>150	Hazra et al. (2018)
Wufeng-Longmaxi	Sichuan Basin, China	~2.0	8, 20, 60, 100, 200	100–200	Zhang et al. (2018b)
Wufeng-Longmaxi	Pengshui area, China	2.48–2.87	4–10, 20–28, 35–48, 60–80, 80–100, 100–115, 115–150, 150–180	60–80	Li et al. (2019)
Wufeng-Longmaxi	Jiaoshiba area, China	~2.5	40–60, 60–80, 80–100, 100–150, 150–200	60–80	He et al. (2021)

To better understand the relationship between sample size and gas-measured pore structure, we propose a conceptual model that integrates these findings (Fig. 6). The most suitable particle size for measurement is defined as the critical particle size. When the sample particles are much larger than this critical size, most nanoscale pores are encapsulated within the mineral matrix (Fig. 6(a)). In this case, the gas can only be adsorbed onto partially exposed pores, leading to an underestimation of the overall pore parameters (Chen et al., 2015; Han et al., 2016). As the particles are progressively ground to smaller sizes, previously closed pores are gradually opened, allowing gas to enter. Although this process often involves the destruction of some pores and the creation of new ones (Fig. 6(b) and (c)), the overall effect is a net increase in accessible pores. Consequently, pore parameters such as pore volume and specific surface area increase and reach their maximum values near the critical particle size. When the particle size becomes smaller than the critical size, however, the number of destroyed pores exceeds the number of newly formed ones

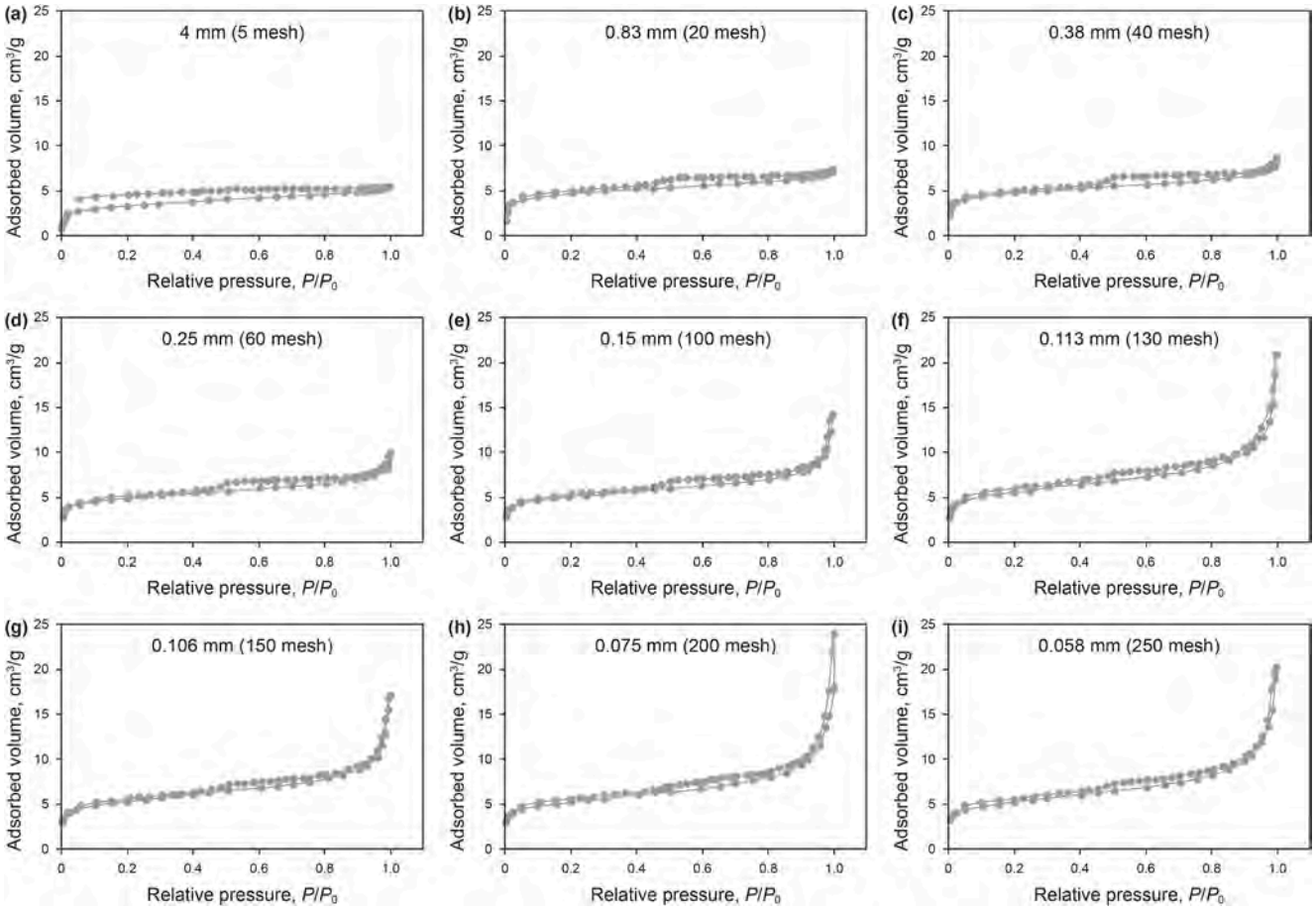

Fig. 4. Low-pressure N_2 adsorption and desorption isotherms with different particle size, modified from Han et al. (2016).

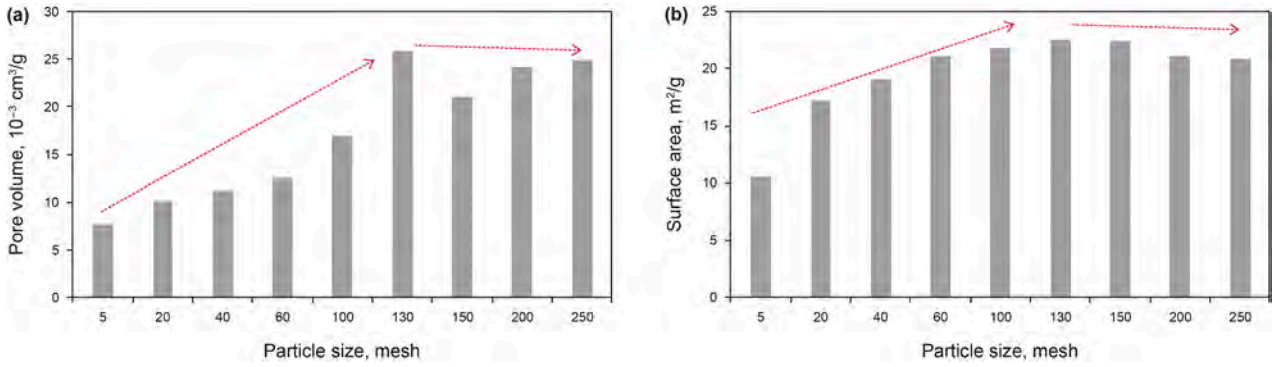

Fig. 5. Influence of particle size on N_2-adsorption pore volume and specific surface area, modified from Han et al. (2016).

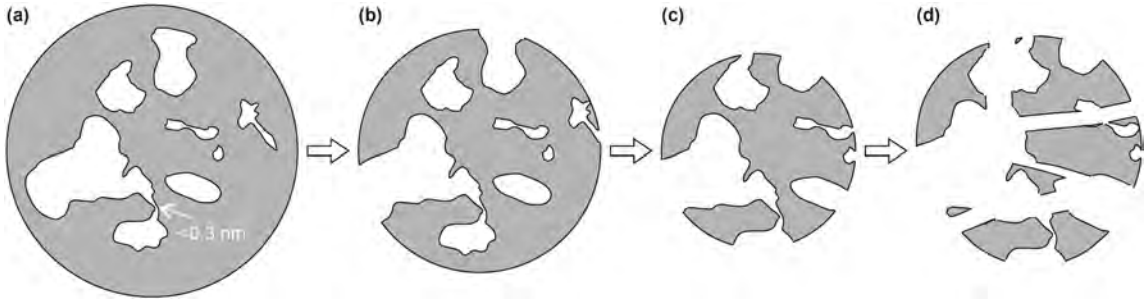

Fig. 6. Schematic diagram depicting detected pore structure changes with particle sizes.

(Fig. 6(d)), again leading to an underestimation of pore structure (Zhang et al., 2018b; He et al., 2021). Therefore, accurately determining the range of critical particle size in gas adsorption experiments is essential for reliable pore structure characterization. Similarly, for experiments such as helium porosity, small-angle neutron scattering (SANS), and pyrolysis parameter measurements of shale rocks (Clarkson et al., 2013; Ruppert et al., 2013; Sun et al., 2016, 2023), which all involve sample crushing, it is equally important to determine the critical particle size required for these experiments along with the corresponding experimental parameters. Currently, these discussions remain incomplete, but they may represent a key issue requiring attention and coordination from multiple perspectives in the future.

Generally, samples are randomly broken during grinding, increasing the difficulty of determining the optimal particle size. Moreover, the heterogeneity of shale can introduce errors during sample preparation and analysis, affecting result reproducibility (Han et al., 2016; Zhang et al., 2018). These factors may contribute to the inconsistencies observed in previous results (Table 2). As a result, there is no universally accepted particle size for gas adsorption studies. A comprehensive review of the literature indicates that particle sizes in the range of 60–150 mesh are widely used and considered valid (Ross and Bustin, 2009; Clarkson et al., 2013; Kuila and Prasad, 2013; Tian et al., 2013; Bertier et al., 2016; Xu et al., 2020a; Gou et al., 2021, 2023; He et al., 2021). To minimize the impact of sample size and heterogeneity, it is essential to combine different characterization methods for cross-verification.

Additionally, the temperature and duration of sample drying before the test, as well as the degree of degassing, can influence the number of gas adsorption sites, thereby affecting the evaluation of the pore structure (Mastalerz et al., 2013). Furthermore, during sample testing, the selection of data points and the equilibration interval time are also crucial factors that require careful attention and standardization. The number of data points and equilibration time determine whether the gas can be fully adsorbed into the pores. Existing literature suggests that the number of data points should exceed 88, and the equilibration time should be greater than 15 s (Liu et al., 2021). This standard has been uniformly adhered to in a large number of studies (Mastalerz et al., 2013; Gou et al., 2019; Sun et al., 2020b). However, it is important to note that both preprocessing parameters (e.g., drying temperature and time) and parameters during the experiment (e.g., data points and equilibration interval) are ultimately determined by the sample size. Smaller sample sizes require shorter drying times, degassing times, and equilibration intervals. This explains why many current studies focus on the significance of sample particle size.

4.2. Selection of the calculation model for gas adsorption

In addition to the confirmed effect of sample particles on N_2 adsorption, the selection of an appropriate calculation model complicates subsequent data processing. Various models are used to quantify pore structure, including the Brunauer-Emmett-Teller (BET), Horvath-Kawazoe (HK), Saito-Foley (SF), Dubinin-Radushkevich (DR), Dubinin-Astakhov (DA), Density Functional Theory (DFT), and Barrett-Joyner-Halenda (BJH) models (Juenger and Jennings, 2001; Groen et al., 2003; Ravikovitch and Neimark, 2006; Neimark et al., 2009; Kuila and Prasad, 2013; Anovitz and Cole, 2015; Bertier et al., 2016). Additionally, the DFT model is further subdivided into Lattice Density Functional Theory (LDFT), Nonlocal Density Functional Theory (NLDFT), and Quenched Solid Density Functional Theory (QSDFT) (Neimark et al., 2009). In particular, the QSDFT model accounts for the surface roughness of porous media and is considered better suited for organic-rich shale (Ravikovitch and Neimark, 2006; Neimark et al., 2009). The BET model is widely accepted for quantifying the specific surface area of shale using N_2 adsorption data (Clarkson et al., 2013; Tinni et al.,

2014a; He et al., 2021). While the HK, SF, DR, and DA models can characterize pore size distribution, they incorrectly assume that the adsorbed phase is a bulk liquid and overlook the inhomogeneity of molecular adsorption in micropores (Kuila and Prasad, 2013; Rouquerol and Rouquerol, 2014). As a result, these models do not accurately reflect the actual micropore filling of the rock, leading to significant errors in micropore size distribution (Thommes et al., 2012). Therefore, the BJH and DFT models are primarily used to estimate pore structure parameters from N_2 adsorption data. The suitability of the DFT versus BJH models for pore volume and size distribution interpretation remains debated, with both models widely used in the literature (Juenger and Jennings, 2001; Bertier et al., 2016; Tang et al., 2016; Li et al., 2019; He et al., 2021).

To further assess applicability, gas adsorption data from the Longmaxi shale in the Jiaoshiba area, China, collected from a previous study, were analyzed (Fig. 7). The samples exhibit similar maturity (R_o ~2.5%) but vary in TOC content and mineralogy (Xu et al., 2020a). The pore volume distribution obtained through N_2 adsorption, analyzed by the DFT model, shows high similarity across samples, with only slight variations in absolute values. The largest pore size is approximately 50 nm (Fig. 7(a), (d), (g)). The pore volumes of siliceous-rich shale (S-3), mixed shale (M-2), and argillaceous-rich shale (CM-1), calculated using the DFT model, are 21.6×10^{-3}, 15.8×10^{-3}, and 12.5×10^{-3} cm^3/g, respectively. In contrast, the BJH model reveals significant differences among the shale samples, with pore sizes reaching approximately 300 nm (Fig. 7(b), (e), (h)). The BJH model's evaluation is consistent with observations from Xu et al. (2020a) based on SEM images, which indicate that S-3 shale developed numerous OM pores in the nanometer to submicron range. In contrast, CM-1 shale was primarily characterized by pores related to sub-micron clay minerals. These differences in pore size distribution are also more aligned with the theoretical expectations for different rock lithofacies. The pore volumes of S-3, M-2, and CM-1, as calculated by the BJH model, are 30.9×10^{-3}, 23.9×10^{-3}, and 24.6×10^{-3} cm^3/g, respectively (Fig. 7). Moreover, previous studies, including Helium pycnometry and MICP experiments, have shown that the pore volume of S-3 shale in the Jiaoshiba area is typically above 30×10^{-3} cm^3/g, while CM-1 shale tends to be around 20×10^{-3} cm^3/g (Jiang et al., 2016; Yang et al., 2018; Shu et al., 2020). This further suggests that the BJH model's evaluation results are relatively more reliable. At a pore size of approximately 1 nm, the BJH model indicates a downward trend, reaching a relatively low value at around 1.5 nm. For example, for M-2 shale, when the pore diameter is approximately 1.5 nm, the pore volume identified by the BJH model is 0.16×10^{-3} cm^3/g, while the DFT model identifies a pore volume of 0.06×10^{-3} cm^3/g. Therefore, the pore volume determined by the BJH model aligns more closely with the volume identified by CO_2 adsorption at a pore diameter of approximately 1.5 nm (0.14×10^{-3} cm^3/g).

Although the pore structure calculated by BJH model relies on the Kelvin equation and may provide less information about micropores than the DFT model, we suggest that the BJH model is preferable for interpreting N_2 adsorption for two main reasons: 1) CO_2 analysis is commonly used to characterize micropores and complements the N_2 method (Fig. 7) (Anovitz and Cole, 2015; Bertier et al., 2016), and 2) the pore diameters of typical shales in commercial development are predominantly greater than 10 nm (Nelson, 2009; Arif et al., 2021; Jiang et al., 2023). Importantly, macropore information, assessable through N_2 adsorption (Groen et al., 2003; Anovitz and Cole, 2015), is only revealed by the results from the BJH model (Fig. 7). It is important to note that the conclusions drawn here are preliminary, and further research—particularly on shales with varying maturity and preservation conditions—is needed before definitively concluding the significance of the BJH model.

4.3. Is Ar-ion-beam milling required

Ar-ion-beam milling is widely used to polish shale surfaces prior to SEM imaging analysis (Milliken and Curtis, 2016; Sanei and Ardakani, 2016). Loucks et al. (2009) reported that Ar-ion-beam milling improves stacking artifacts caused by the differential hardness of sample components. This technique produces flat surfaces, enabling high-quality and undistorted SEM imaging for nanopore characterization (Loucks et al., 2009; Curtis et al., 2012a; Mastalerz and Schieber, 2017; İnan et al., 2018). However, several adverse effects of ion milling have been documented (Grobe et al., 2017; Mastalerz and Schieber, 2017; İnan et al., 2018). Ion bombardment induces multiple interactions between ions and the sample surface, particularly in very small sample pieces (Sanei and Ardakani, 2016). The implantation and sputtering of ion energy, coupled with heating from the ion beam, can alter the sample surface (Grobe et al., 2017; Mastalerz and Schieber, 2017). Heat accumulation is more pronounced on samples with low conductivity (e.g., organic matter) than on those with high conductivity (e.g., minerals) (Sanei and Ardakani, 2016). Sanei and Ardakani (2016) observed that the reflectance (R_o) of solid bitumen increased from 0.52% to 0.79% (a 53% increase) after Ar-ion-beam milling (Fig. 8(a) and (b)). This thermal change corresponds to an increase in burial temperature of approximately 50 °C. Similarly, Mastalerz and Schieber (2017) found R_o increased from 0.27% to 0.45%, a 66% rise. Higher energy, focused ion beam (FIB) milling can further amplify this effect (Fig. 8(c)) (Sanei and Ardakani, 2016). Ion milling can also create artificial porosity due to the rapid devolatilization of lighter organic compounds in macerals (Sanei and Ardakani, 2016; Grobe et al., 2017; Mastalerz and Schieber, 2017; Katz and Arango, 2018). İnan et al. (2018) reported that pores appeared more numerous and larger in ion-milled samples (R_o ~1.43%) (Fig. 9(a) and (b)).

Our study of overmature siliceous-rich shale (R_o ~2.5%) from the Longmaxi Formation in the Jiaoshiba area, China, shows that SEM images after Ar-ion-beam milling exhibit fewer scratches and less surface waviness, resulting in improved surface quality (Fig. 9(c)–(f)). Ion milling did not significantly alter pore distribution, shape, or size but made these features more visible (Fig. 9(c)–(f)). The oil-prone kerogen in such mature samples is highly aromatic and resistant to heating (Mastalerz et al., 2013; Mastalerz and Schieber, 2017). Although the overmature shales in our study showed no significant changes in pore structure, Sanei and Ardakani (2016) reported that the R_o of pyrobitumen increased from 2.16% to 2.38% after ion-beam milling at 6 kV. Thus, intense ion milling should be avoided, even for higher-maturity samples, to prevent surface changes (Mastalerz and Schieber, 2017).

Given that intense ion milling causes volatile expulsion and thermal alteration of organic matter (Sanei and Ardakani, 2016; Mastalerz and Schieber, 2017), which can significantly affect pore characteristics (Milliken and Curtis, 2016), the suitability of ion milling for lower-maturity shale is questionable. Based on our SEM observations, we suggest that mechanical grinding and polishing may provide more accurate results. However, we do not propose mechanical grinding and polishing as a substitute for ion milling, as some institutions have successfully adjusted ion milling parameters to mitigate its effects. For example, the Beijing Research Institute of Uranium Geology uses a cycle of polishing for 20 min at 5 kV, followed by a 10-min pause, repeated three times. This method saves costs and time while improving sample quality.

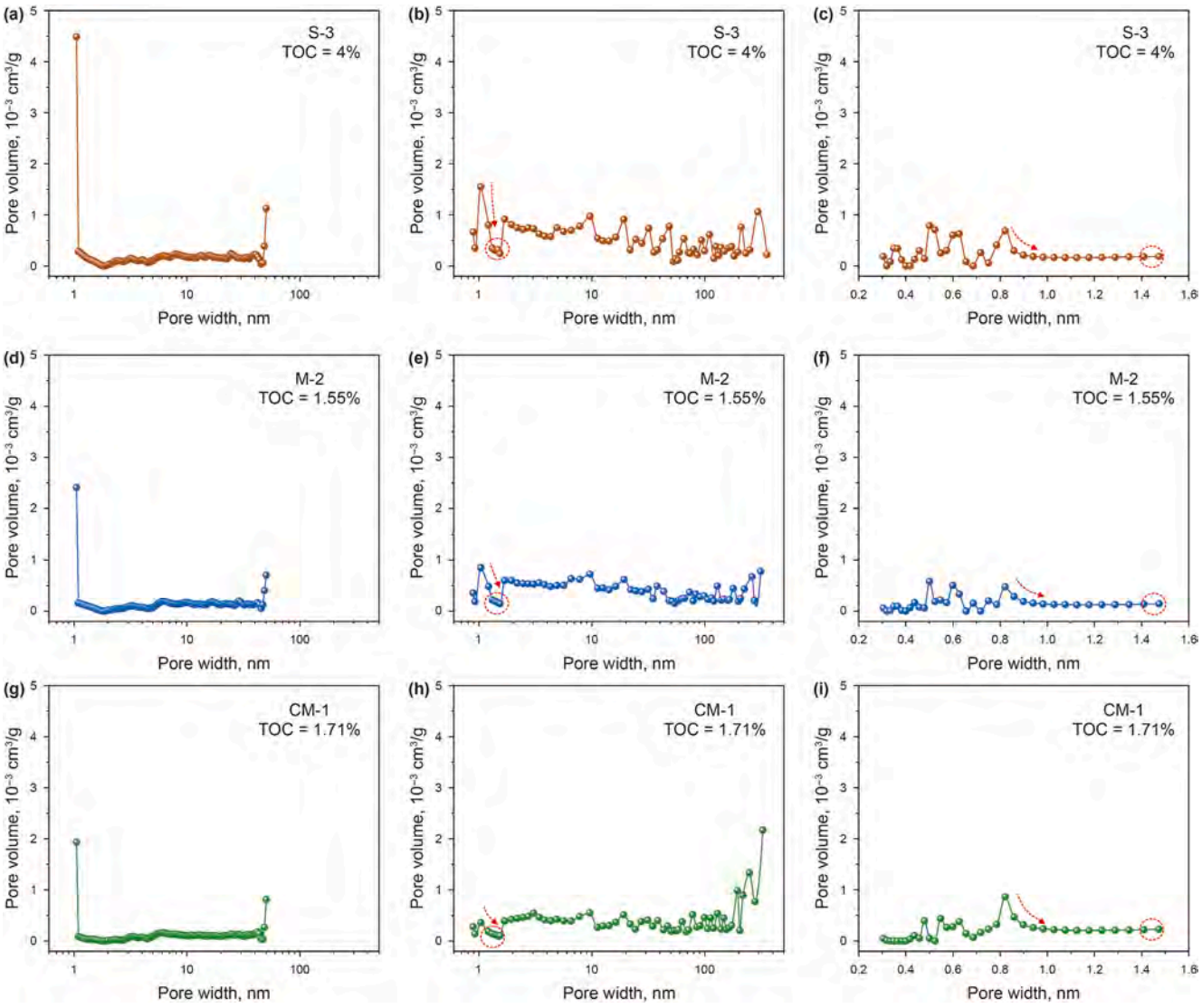

Fig. 7. Comparison of pore size distribution obtained from N_2 and CO_2 adsorption. **(a)**, **(d)**, and **(g)** are obtained from N_2 adsorption, calculated by the DFT model; **(b)**, **(e)**, and **(h)** are obtained from N_2 adsorption, calculated by the BJH model; **(c)**, **(f)**, and **(i)** are obtained from CO_2 adsorption, calculated by the DFT model. Gas adsorption data are modified from Xu et al. (2020a). S-3: siliceous-rich shale lithofacies; M-2: mixed shale lithofacies; CM-1: argillaceous-rich shale lithofacies.

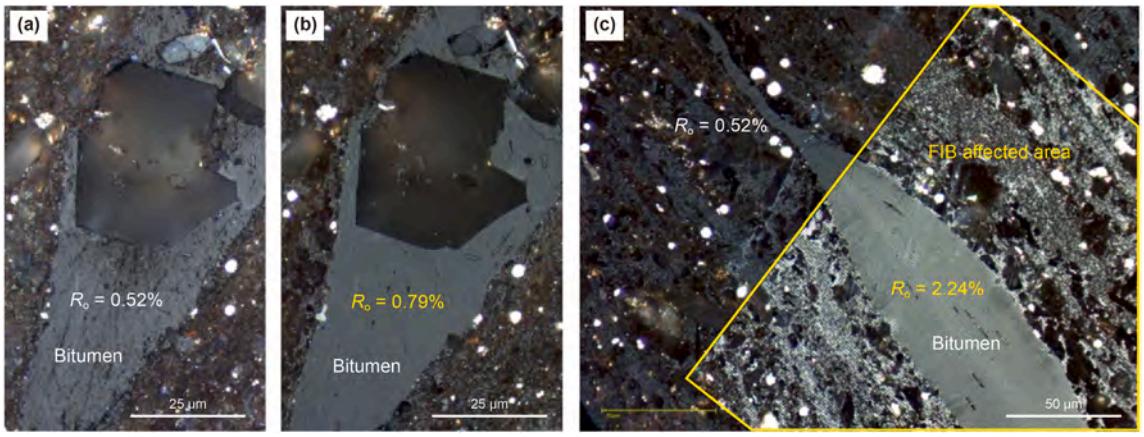

Fig. 8. Influence of ion beam polishing on solid bitumen, modified from Sanei and Ardakani (2016). **(a)** Solid bitumen before ion polishing; **(b)** solid bitumen after cryogenic broad ion beam polishing, R_o is enhanced; **(c)** R_o of bitumen is significantly increased after focused ion beam polishing.

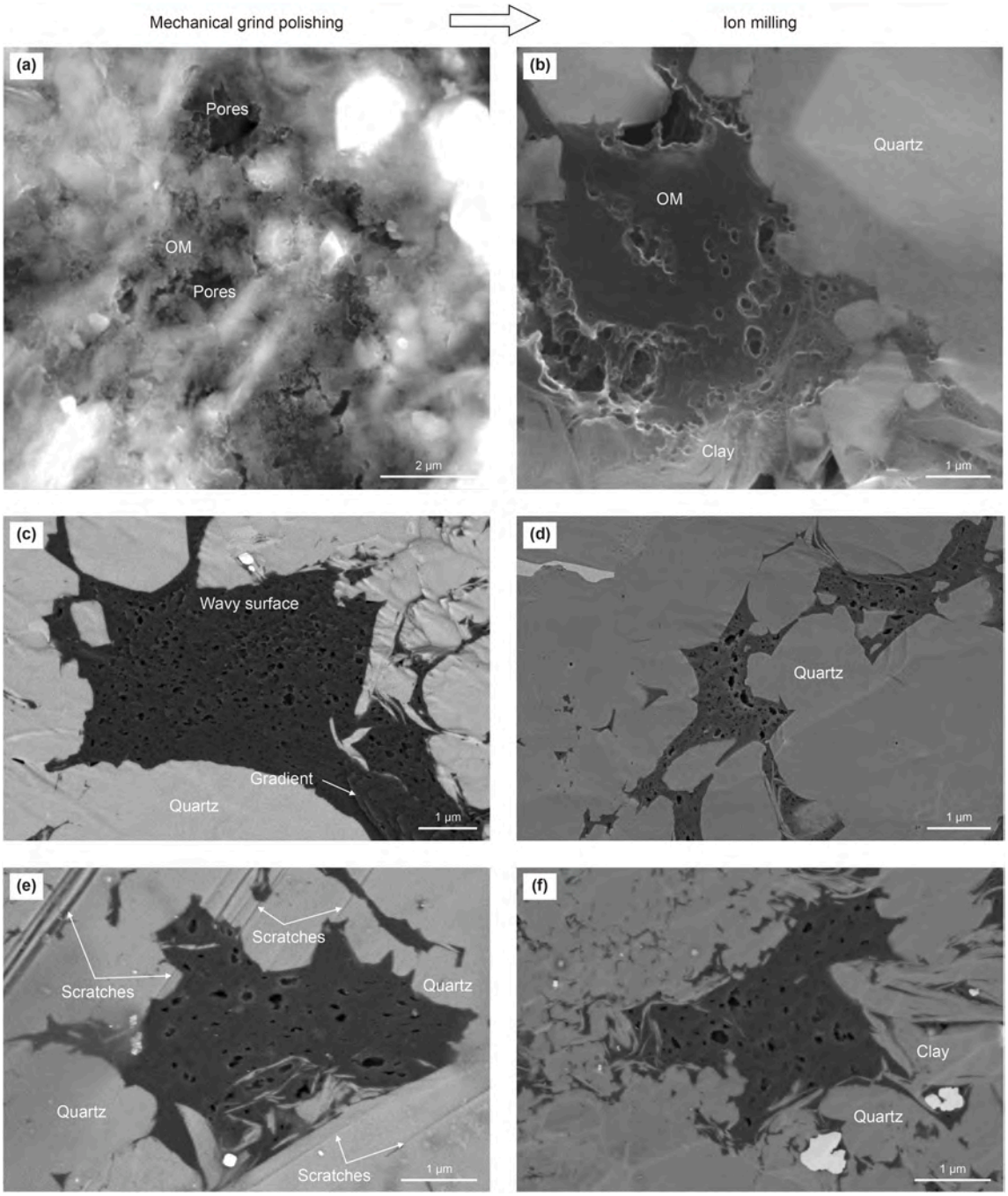

Fig. 9. Difference between mechanically polished surfaces and Ar-ion-beam milling surfaces. **(a)–(b)** show samples with R_o of ~1.43%, modified from İnan et al. (2018); **(c)–(f)** show samples with R_o of ~2.5%.

4.4. Observation conditions for FE-SEM

Scanning electron microscopy (SEM) is a key experimental technique for shale reservoir characterization. While it offers significant opportunities, it also presents several challenges. In addition to ion milling, experimental observation conditions—such as acceleration voltage, current, and dwell time of the electron beam—pose further challenges (Wang et al., 2015b; Zhao et al., 2019).

Acceleration voltage refers to the potential difference between the anode and cathode of the electron gun, which determines the energy of the incident electron beam. This, in turn, affects the penetration depth of the electrons (Hua et al., 2014). A higher acceleration voltage increases electron energy, leading to deeper penetration into the sample surface (Imbraguglio et al., 2012; Tomkus et al., 2020). While this can reduce surface contamination and facilitate the observation of internal characteristics, it may also cause negative effects, such as the loss of microstructural details on the sample surface (Fig. 10(a)–(d)).

Generally, the incident electron current (I_p) in SEM is typically the sum of the backscattered electron current (ηI_b), secondary electron current (δI_b), and ground current (I_{sc}) (Hua et al., 2014; Wang et al., 2015b). When the sum of the secondary electron yield (δ) and backscattered electron yield (η) exceeds 1, grounding

effects cause excess electrons to be discharged, forcing $\delta + \eta$ to approach 1 (Wang et al., 2015b; Song et al., 2021). However, when the voltage is $<V_1$ or $>V_2$ (i.e., $\delta + \eta < 1$), large charges will accumulate on the sample surface, producing charging effects (Fig. 11). This can distort the sample information (Tomkus et al., 2020). In practice, both current and voltage are adjusted during SEM observation. Increasing the current improves resolution but also leads to charge accumulation and potential loss of information (Fig. 10(a)–(d)). Zhao et al. (2019) suggested that a voltage <10 kV and a current <170 pA are optimal for pore characterization and subsequent post-processing analysis (e.g., OM surface porosity statistics, Song et al., 2019; Xu et al., 2020a). Additionally, extending the scanning time can improve the signal-to-noise ratio and image quality. However, this also increases the dwell time of the electron beam, risking image distortion and high-brightness tailing (Fig. 10(e) and (f)). It is important to note that although this charge accumulation may not be ideal for image analysis, it can have specific applications, such as revealing the distribution of residual oil in reservoirs (Wang et al., 2015b).

As discussed, these three factors—voltage, current, and dwell time—jointly control the quality of SEM images, which in turn affects the extraction and interpretation of pore characteristics (Klaver et al., 2012; Gou et al., 2019; Chandra and Vishal, 2021). Excessive experimental conditions can cause significant electron bombardment, leading to sample heating, similar to ion polishing, and altering the pore structure (Imbraguglio et al., 2012; Tomkus et al., 2020). This phenomenon has also been observed in our SEM image analyses. Therefore, selecting appropriate conditions is crucial for obtaining accurate shale pore information. We recommend starting with a moderate acceleration voltage (e.g., 3–5 kV) and adjusting the parameters based on the specific sample characteristics. Lower voltage, current, and dwell time are more suitable for samples with a high matrix mineral content. For samples with higher clay or organic matter content, these parameters may be increased to achieve a more comprehensive and accurate understanding of the pore structure. For example, the samples shown in Fig. 9(d) and (f) are shale with approximately 60% felsic minerals and a TOC of about 3%. For these samples, we used a voltage of

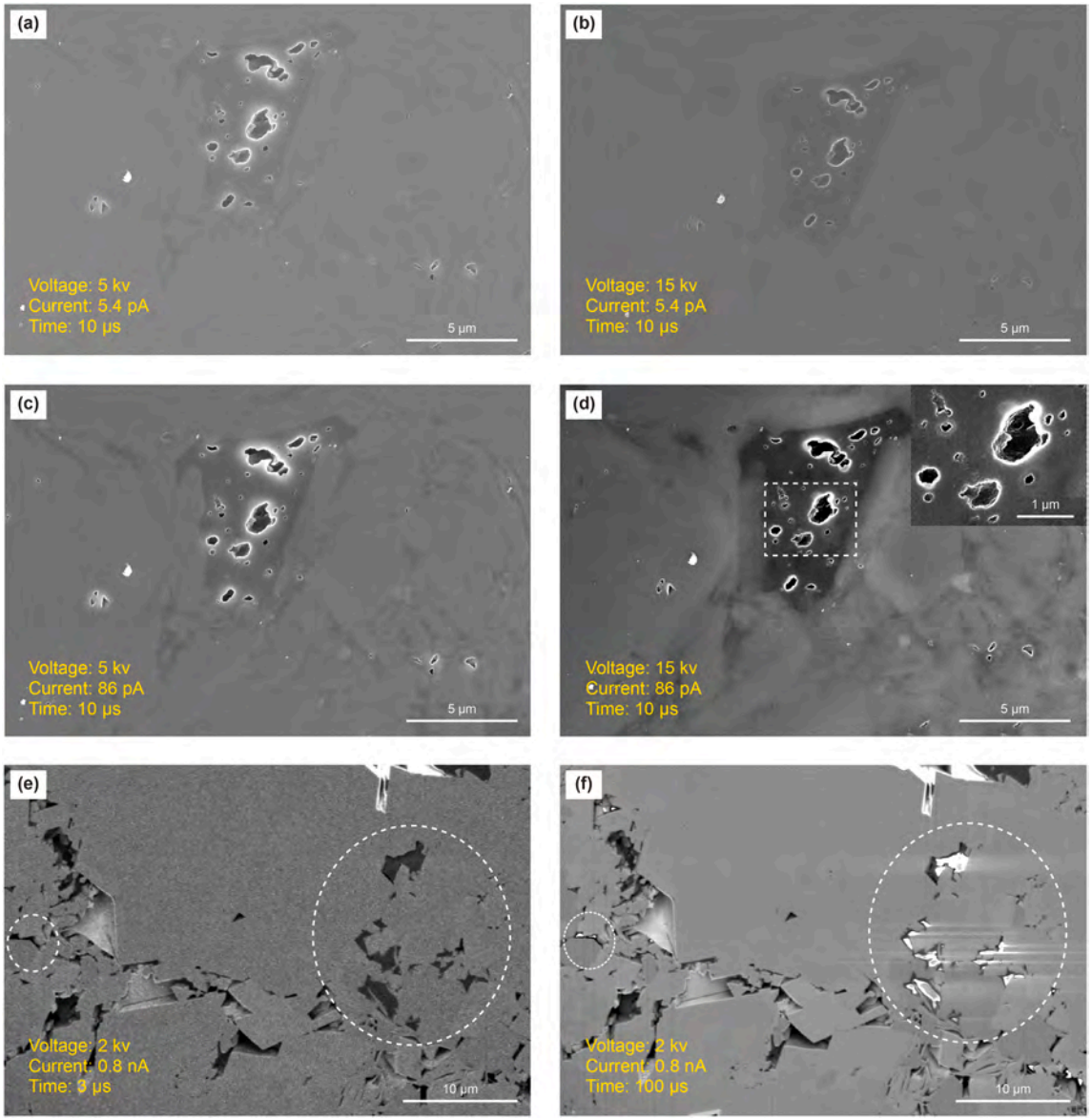

Fig. 10. Influence of voltage, current, and residence time on quality of SEM images. **(a)–(d)** are modified from Zhao et al. (2019), **(e)–(f)** are modified from Wang et al. (2015b).

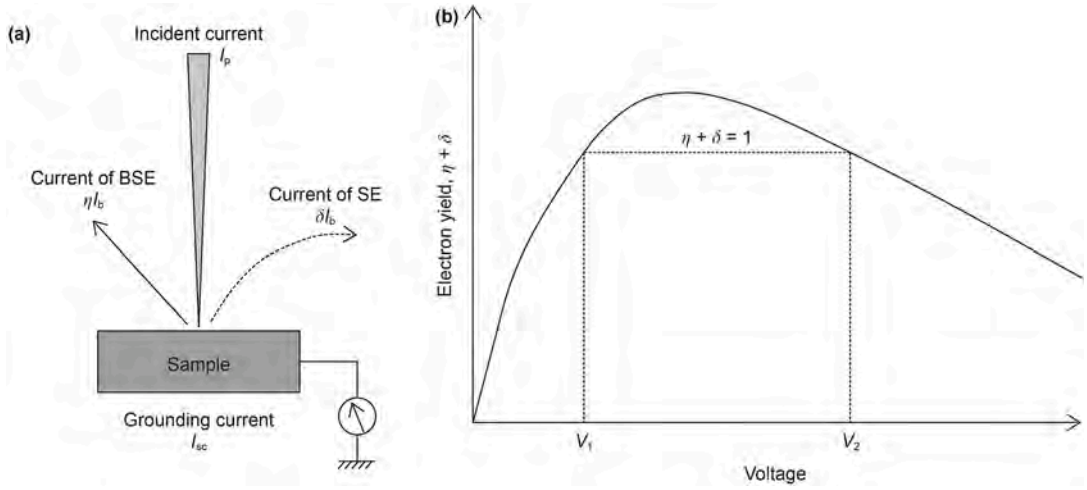

Fig. 11. Generation mechanism of charging in sample surface, modified from Hua et al. (2014) and Wang et al. (2015b). η: backscattered electron (BSE) yield; δ: secondary electron (SE) yield.

3 kV, a current of 0.4 nA, and a dwell time of 30 μs, resulting in excellent imaging (Fig. 9(d), (f)). In contrast, for samples with a higher clay mineral content, we found that adjusting the voltage to 5 kV could achieve an imaging effect similar to the one above. However, it is important to note that this conclusion is preliminary, based on a limited number of tests conducted during our work. In SEM detection, several factors, including the type of instrument, whether the sample is coated with carbon or gold, the degree of sample drying, and the hydrocarbon content, all influence the optimal parameter settings.

4.5. Three-dimensional imaging

Following the acquisition of 2D greyscale images by CT scanning, these images are superimposed to produce a 3D data volume (Wu et al., 2019, 2020b). In a CT scan image, the gray value represents the density of the substance. Transitioning from black to white signifies a density shift from low to high (Gou et al., 2019). Substances with higher density (e.g., pyrite) appear brighter in the CT image. Pores and micro-fractures appear nearly black or with lower gray values (Wang et al., 2016). This allows for the analysis of pore structure by interpreting color variations in the image. Filters are vitally necessary to apply to original images to reduce noise and chromatic aberration, making pore phases more visible (Ma et al., 2017; Chandra and Vishal, 2021). There are many filters that can be used for shale images, and their filtering effects differ significantly (Buades et al., 2006; Saif et al., 2017). The filtering effects of various filters on a noisy image are compared and shown in Fig. 12. The non-local-means filter compares the geometric configurations of pixels within the same component, utilizing the self-similarity of images across various locations. It derives the final imaging data through pixel-weighted averaging, demonstrating notable effectiveness in segmenting shale reservoirs with diverse mineral compositions (Buades et al., 2006; Gou et al., 2019). Therefore, the noise removed by the non-local-means filter is more noticeable (Fig. 12(a1)–(a4)). However, with the increase in filtering times, small pore information is gradually removed (Fig. 12(a4)). The anisotropic diffusion filter emphasizes the retention of straight edges (Buades et al., 2006), and thus the noise removal effect is relatively weak (Fig. 12(b1)–(b4)). When the delineate filter is applied to the raw image, noise and multiphase component information in shale are depicted simultaneously (Ma et al., 2017; Saif et al., 2017). The superposition of artifacts makes it difficult to extract useful information (Fig. 12(c1)–(c4)). The Gaussian filter method blurs pixels to remove noise, and a 2D convolution operator is performed during this process (Buades et al., 2006; Chandra and Vishal, 2021). Overall, the slice after the third filtering is almost unchanged from the original slice (Fig. 12(d1)–(d4)). The box filter uses deconvolution to extract material phases from high-noise images (López et al., 2022). While the noise is removed, the virtual shadow caused by the loss of potential dependencies between estimated components becomes gradually obvious (Fig. 12(e1)–(e4)). Apart from these, the median filter and edge-preserving smoothing filter are also commonly mentioned (Buades et al., 2006; Ma et al., 2017; Chandra and Vishal, 2021). Each method provides reasonable solutions, but none is perfect. Applying a combination of these filters on a case-by-case basis may be an effective way to minimize noise and retain useful information. This is a task that requires long-term attempts and improvements by scholars.

During the operation of FIB-SEM, the ion beam mills and polishes the surface of the sample, while the electron beam is used for imaging (Curtis et al., 2012b; Fitschen et al., 2017). However, due to different sputtering rates of the ion beam and incomplete milling of the material, the resulting images often possess a curtaining effect, i.e., bright stripe-like artifacts (Fig. 13). There are two ways to deal with this problem. One is to use a lower beam current, which leads to impractical processing times and increased costs. The other is to discard this part of the images, which may compromise representativeness. Currently, the Fast Fourier Transform (FFT) filter in Avizo (https://www.fei.com/software/avizo3d/) is a simple method to remove the curtain effect (Schankula et al., 2018; Mahmoud et al., 2023). The results presented in our work are also very effective (Fig. 13). In light of this, we further analyzed the pore characteristics of the images before and after removing the curtaining effect. As shown in Fig. 13, all images were processed according to a standardized procedure. However, the proportion of pore development in the image without removing the curtaining effect was significantly higher. This discrepancy arises because the artifacts caused by the curtaining effect were included in the analysis, leading to increased error. Therefore, effectively removing the curtaining artifacts in SEM images is crucial for constructing the three-dimensional dataset for FIB-SEM and accurately capturing its internal pore information. It is worth noting that Fourier-based filtering, moment matching, and histogram-based methods have

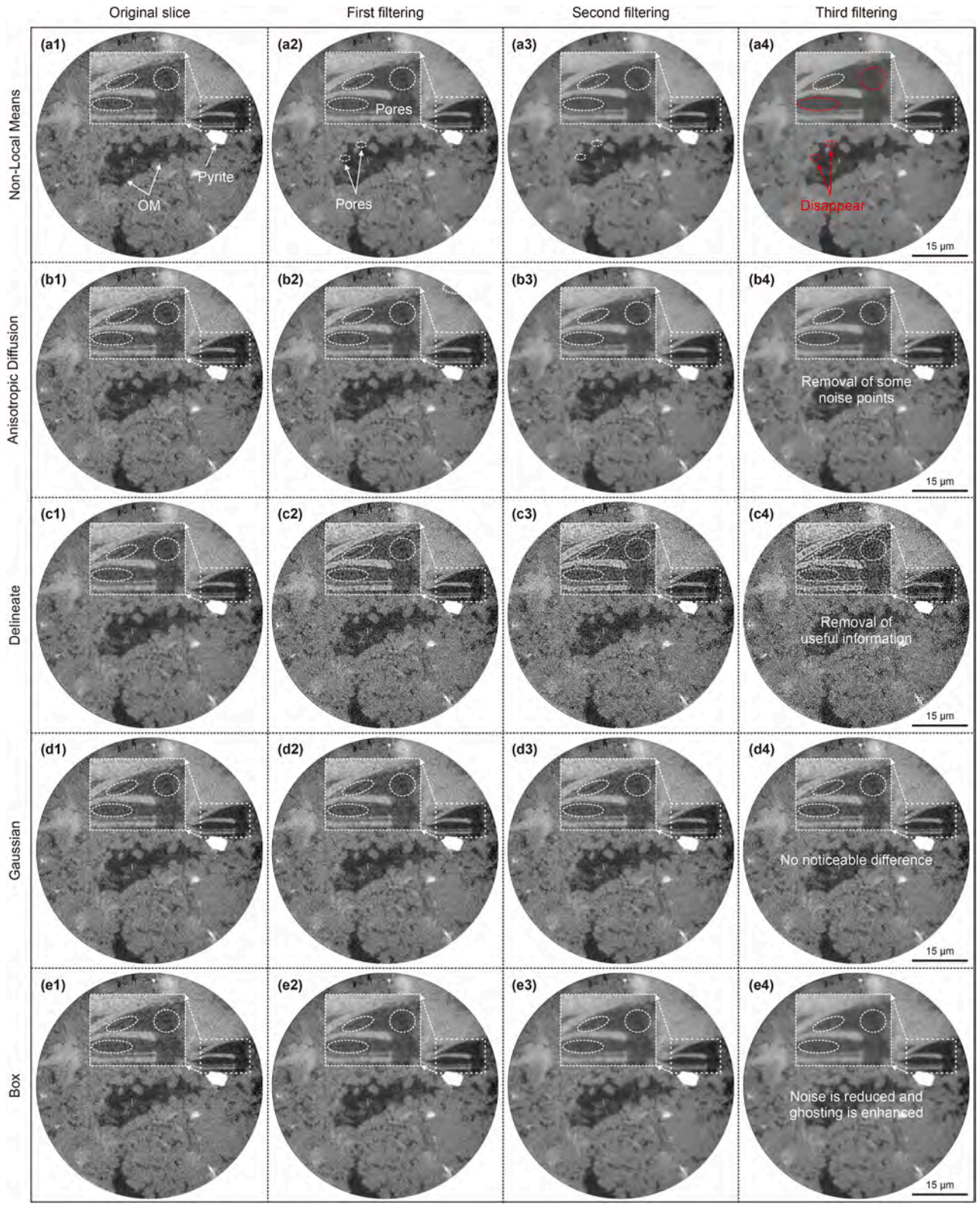

Fig. 12. Comparison of the effects of different filters and the number of filtering operations on noise removal and pore presentation in CT slices. **(a1)–(e1)** show the original images without any processing, with the dotted box highlighting potential pores; **(a2)–(e2)** show CT slice images after one filtering operation; **(a3)–(e3)** show CT slice images after two filtering operations; **(a4)–(e4)** show CT slice images after three filtering operations. In **(a4)**, the red dotted box in the center indicates the area where pores have disappeared after multiple filtrations.

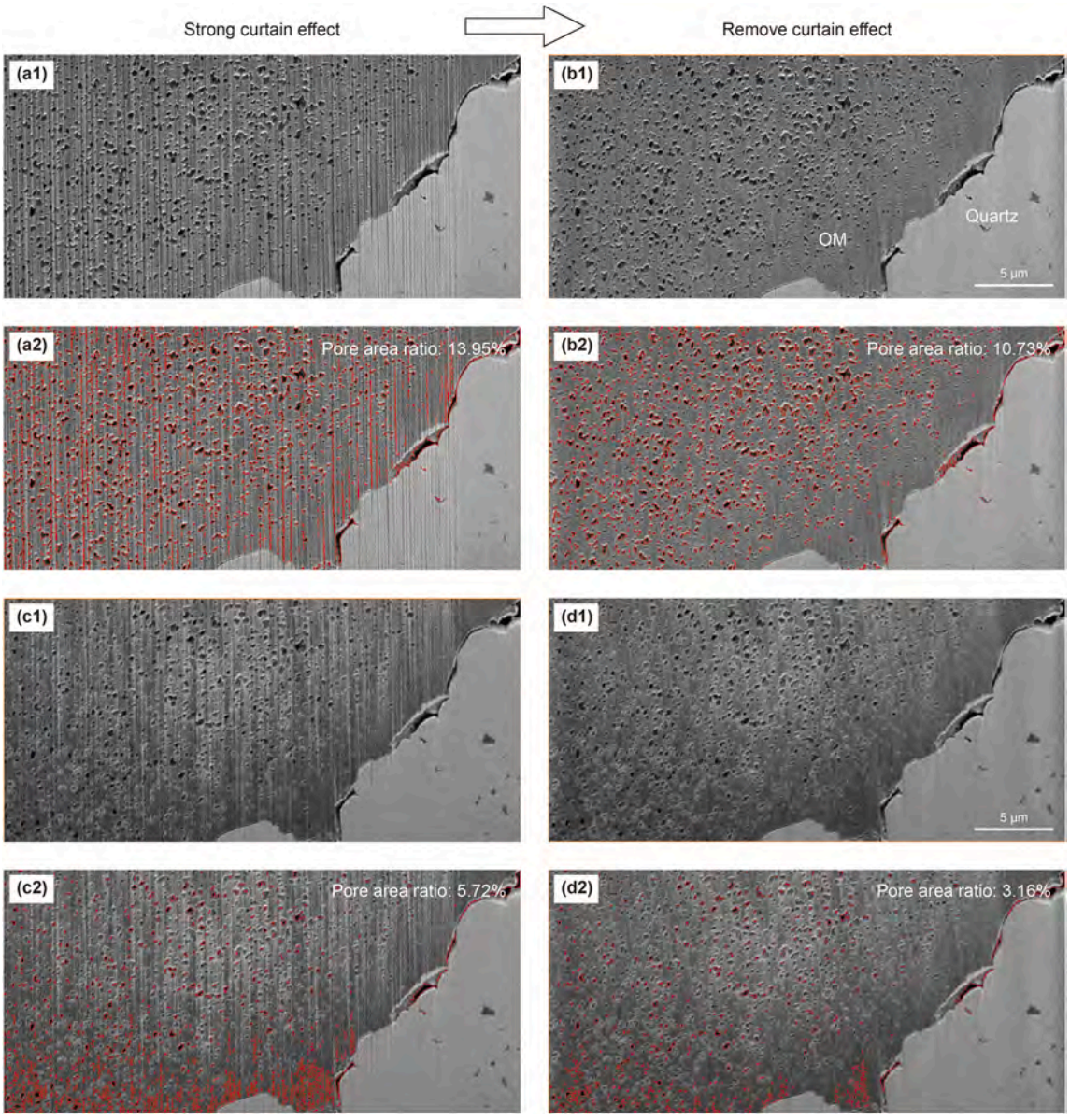

Fig. 13. An example of using the FFT model to remove the curtain effect from FIB-SEM images **(a1)–(d1)** and to eliminate its influence on the pore statistics results **(a2)–(d2)**. The red area represents the pores delineated using a unified standard. The pore area ratio refers to the proportion of the red area relative to the total area of the image.

also been suggested in the relevant literature (Chen and Pellequer, 2011; Fitschen et al., 2017). The ultimate goal is to obtain high-quality images and accurately evaluate the characteristics of shale reservoirs.

5. Prospects and challenges: pore structure fine characterization

5.1. Quantitation of reservoir space for different types

From the perspective of pore types, the reservoir space in shale can be broadly classified into two categories: inorganic and organic pores. Inorganic pores include interP pores, intraP pores, and fracture-related pores (Fig. 2), and they serve as key reservoir spaces for free gas (Gou and Xu, 2019). The internal surface area of OM pores is significantly higher than that of inorganic pores, providing more adsorption sites, which facilitates the storage of adsorbed gas (Bernard et al., 2013; Hao et al., 2013). Furthermore, if the number of organic pores is sufficiently high and their sizes are large enough, substantial amounts of free gas can also be stored in the central regions of the pores after gas adsorption is completed (Jin et al., 2021; Abolghasemi and Andersen, 2022; Cai et al., 2024; Wu et al., 2024). Due to the more complex pore network in OM pores, gas flow within them is relatively restricted (Hu et al., 2015; Cai et al., 2024). Therefore, clearly distinguishing and evaluating the content of OM and inorganic pores not only enhances the accuracy of reservoir assessments but also guides exploitation and engineering applications, ultimately improving the development efficiency and economic benefits of shale gas.

The fitting slope method is a widely used and efficient approach for calculating organic and inorganic porosity (Ma et al., 2016; Chen et al., 2019). This method relies on the strong positive correlation between TOC content and porosity. In general, inorganic

porosity is estimated as the intercept when the TOC content is zero, based on the linear relationship (Fig. 14(a) and (b)). Given this, organic porosity can be calculated by subtracting the inorganic porosity from the total measured porosity. However, we observed that the measured porosity at some points is lower than the estimated inorganic porosity (Fig. 14(a) and (b)), suggesting that the validity of the assessed results may be overly optimistic, at least for these points. Furthermore, two additional limitations should be noted. First, the evaluation results are highly dependent on the number of data points. Changes in the number of data points can alter the linear relationship, thereby affecting the porosity results. Second, there may be no clear relationship between TOC and porosity in highly deformed areas (Xu et al., 2020a; Gou et al., 2021) or in regions with limited thermal maturity (Dong and Harris, 2020), rendering this method inapplicable. Overall, the porosity of both organic and inorganic pores evaluated by this method is constrained by factors such as the amount of data and the degree of correlation between TOC and porosity. Consequently, although this method is relatively simple, the calculated results often exhibit considerable errors.

Using the mass balance principle, Wang et al. (2014) developed a petrophysical model to quantitatively analyze the components of shale porosity (Fig. 14(c)). In this model, shale pore spaces are categorized into pores associated with brittle minerals, pores related to clay minerals, and organic pores. The porosity of a shale reservoir can then be expressed using Equation (1). In principle, this model provides a reliable method for evaluating porosity characteristics and has been widely applied in the literature (Gou et al., 2020; Shu et al., 2020). However, subsequent studies have highlighted that the influence of mineralogy and TOC on shale pore space is far more complex, involving interactions between organic matter and inorganic minerals (İnan et al., 2018; Katz and Arango, 2018). Therefore, this model is more applicable to shales in the middle and late diagenetic stages, where the pore system is relatively stable. It is also important to note that the calculated organic porosity values for argillaceous shales may be overestimated, as the model was developed for organic-rich shales (TOC >2%) (Wang et al., 2014). Nonetheless, the method has been widely used for the quantitative analysis of various types of porosity in shale gas reservoirs, particularly in the complex regions of southern China (Wang et al., 2014; Gou et al., 2020; Shu et al., 2020). This suggests that the model may be one of the most accurate and practical approaches available.

$$\Phi = \rho \times A_{\mathrm{Bri}} \times V_{\mathrm{Bri}} + \rho \times A_{\mathrm{Clay}} \times V_{\mathrm{Clay}} + \rho \times A_{\mathrm{TOC}} \times V_{\mathrm{TOC}} \quad (1)$$

where Φ is the porosity of the shale sample, %; ρ is the bulk density of the shale sample, g/cm^3; A_{Bri}, A_{Clay}, and A_{TOC} are the mass fractions of brittle mineral, clay, and organic matter, respectively, %; V_{Bri}, V_{Clay}, and V_{TOC} are the pore volume of per unit mass of brittle mineral, clay, and organic matter, respectively, cm^3/g.

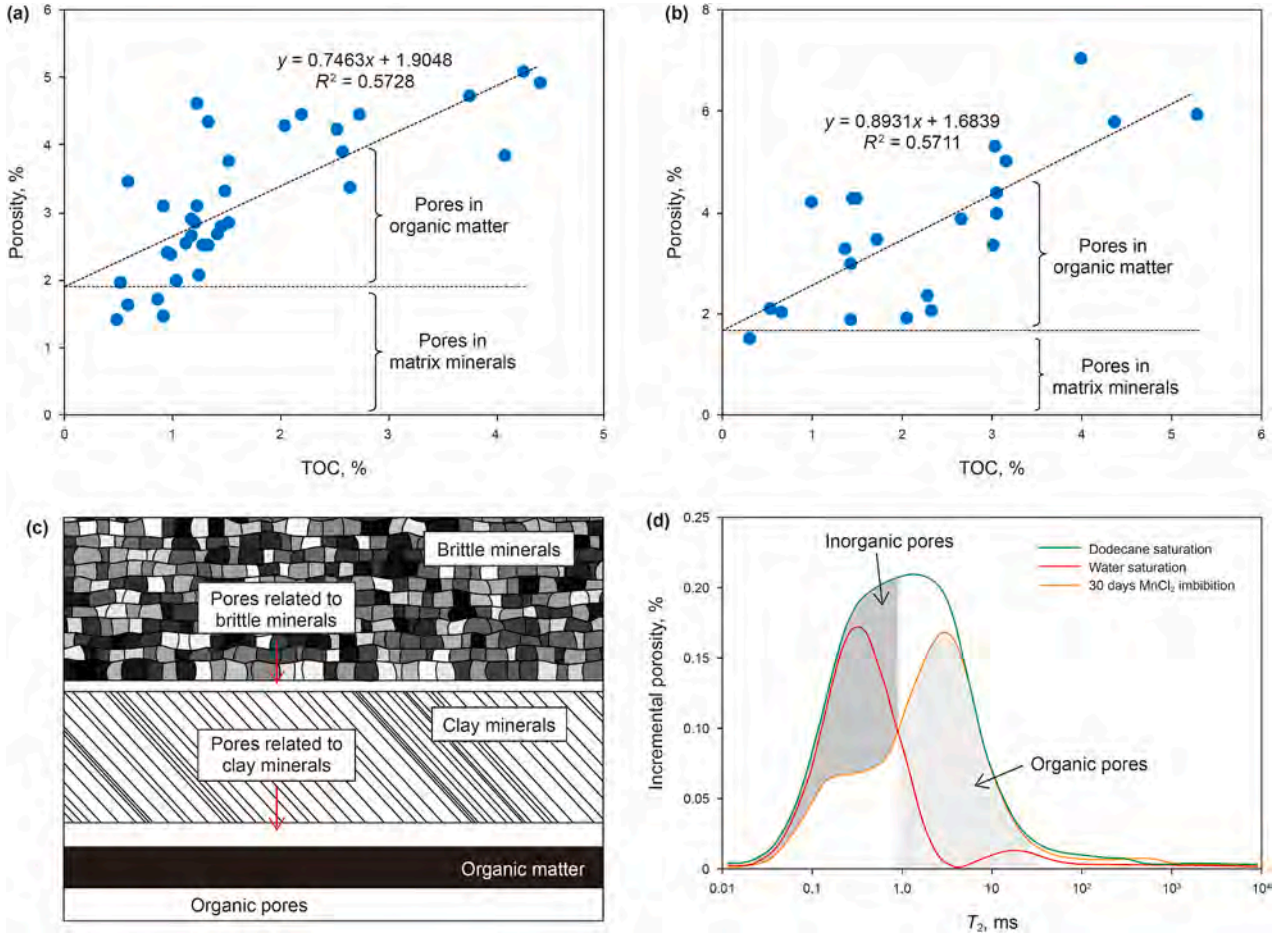

Fig. 14. Evaluation of organic and inorganic porosity with different methods. **(a)–(b)** are calculated by the relationship between TOC and shale total porosity, modified from Ma et al. (2016) and Shu et al. (2020); **(c)** is calculated by a rock physical model, modified from Wang et al. (2014); **(d)** is calculated by an NMR spectrum, modified from Gannaway (2014).

Nuclear magnetic resonance (NMR) has also been employed to characterize the porosity components of shale (Fig. 14(d)) (Gannaway, 2014; Yao and Liu, 2018). Tinni et al. (2014b) demonstrated that brine can infiltrate both organic and inorganic pore systems at pressures below 7000 psia, whereas dodecane fails to penetrate clay pores even at higher pressures. Gannaway (2014) further confirmed that dodecane enters only the organic pores. Since inorganic pores are water-wettable, water-saturated samples typically exhibit strong NMR T_2 spectrum signals in these pores (Sulucarnain et al., 2012; Lai et al., 2018). The distinct contrast between various T_2 spectra ultimately enables the quantification of porosity partitioning in shales (Fig. 14(d)) (Sulucarnain et al., 2012; Gannaway, 2014; Tinni et al., 2014b). As noted earlier, shale saturation with water can alter the pore structure due to expansion, which impacts the accuracy of the results (Sun et al., 2020a; Jiang et al., 2023). Moreover, NMR testing parameters—such as waiting time, echo time, and the number of echoes—directly influence the accuracy and reliability of reservoir characteristics, including porosity and pore size distribution. Different lithologies require distinct testing parameters (Zhang et al., 2018a; Song and Kausik, 2019; Bai et al., 2023). However, these parameters vary significantly across different testing processes, and no standardized approach has been established. The determination of organic and inorganic pore porosity through NMR remains subject to significant uncertainty, and the associated methods and parameters require further refinement.

In addition to the aforementioned methods, porosity partitioning between organic and inorganic pores can be quantified by processing 2D SEM images (Loucks et al., 2009; Milliken et al., 2013; Song et al., 2019). The core of this method lies in the statistical analysis of organic pores in 2D images. However, the resolution limit of SEM (~2 nm) and inherent statistical errors (Chandra and Vishal, 2021) may sometimes yield inconclusive results. Resolution also poses a challenge when differentiating organic and inorganic pores using 3D imaging techniques (Gou et al., 2019; Arif et al., 2021). Additionally, some researchers have proposed using logging data (Zhang et al., 2019) and geochemical parameters (Zhang et al., 2021) to quantify organic and inorganic pores. However, many parameters in these models are difficult to accurately determine. In summary, while numerous methods exist to quantify porosity partitioning in shales, all of them involve multiple variables. These factors increase the potential uncontrollability of calculation errors and limit their applicability.

5.2. Full-scale analysis of pore space

The integrated characterization of shale pore structure is crucial for assessing shale enrichment and improving reservoir prediction (Curtis, 2010; Slatt and O'Brien, 2011; Loucks et al., 2012; Hao et al., 2013; Arif et al., 2021). However, the highly anisotropic nature and varied pore sizes of shale complicate accurate quantification (Loucks et al., 2012; Mastalerz et al., 2013; Anovitz and Cole, 2015; Xu et al., 2020a, 2020b). Existing techniques still have notable limitations when used independently (Fig. 1). While challenging, multiscale characterization allows for the identification of overlapping areas between two or more techniques (Fig. 15(a)). Therefore, the combined use of multiscale correlative techniques is widely recognized as an effective solution to this issue (Schmitt et al., 2013; Gou et al., 2019; Wang et al., 2019b; Zhang et al., 2020; Arif et al., 2021; Chandra and Vishal, 2021; Iqbal et al., 2021; Lei et al., 2021).

In recent years, the integration of CO_2 adsorption, N_2 adsorption, and MICP has become a widely adopted method for assessing full-scale pore characteristics of shale reservoirs (Fig. 15(b)) (Schmitt et al., 2013; Jiang et al., 2016; Wang et al., 2019b; Zhang et al., 2020; Iqbal et al., 2021). These studies suggest that shale pore volume is primarily attributed to micropores and mesopores, while macropores and micro-fractures contribute less. However, as mentioned earlier, new micro-fractures and pore damage can occur in highly brittle shale samples during Hg injection at high pressure (Wang et al., 2019a; Sun et al., 2020b). In such cases, Zhu et al. (2016) and Gou et al. (2019) proposed a novel approach that combines gas adsorption with CT scanning (Fig. 15(c)). They demonstrated that the volume proportion of macropores and micro-fractures is comparable to that of micropores or mesopores. The contribution of μm-scale pores to permeability is dominant (Gou et al., 2019). Moreover, imaging technologies enable the evaluation of gas molecule flow mechanisms based on pore distribution (Arif et al., 2021; Chandra and Vishal, 2021).

While these techniques must be integrated to comprehensively describe shale pore spaces and micro-fracture networks, significant challenges remain in combining multiple approaches. For example, there is debate regarding the splicing point of N_2 adsorption and MICP data: should it be 6 nm (Wang et al., 2021), 10 nm (Cao et al., 2016), 50 nm (Jiang et al., 2016; Tang et al., 2016; Wang et al., 2019b; Iqbal et al., 2021), 65 nm (Wang et al., 2019a), 80 nm (Li et al., 2017), or 100 nm (Wang et al., 2015a)? Schmitt et al. (2013) proposed that the connection point should be selected where the variation in pore volume observed by the two techniques is equal. However, such instances are rare (Wang et al., 2019b). Instead, connections are usually established through fixed-

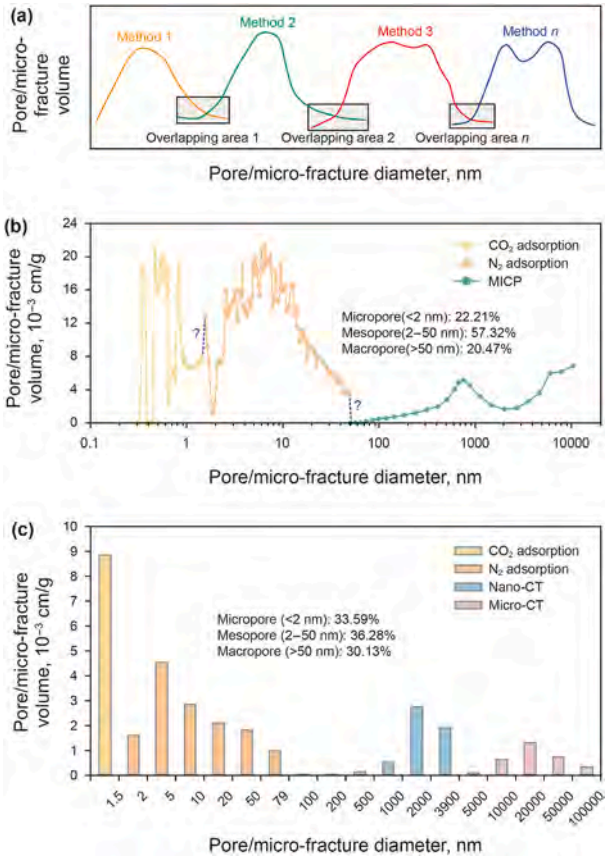

Fig. 15. **(a)** Principle of full-scale pore size distribution using a combination of various methods; **(b)** illustrates the pore size characterization combining CO_2 adsorption, N_2 adsorption, and MICP, modified from Wang et al. (2019b). However, significant discrepancies are evident between the different methods; **(c)** presents the pore size characterization using CO_2 adsorption, N_2 adsorption, nano-CT, and micro-CT, modified from Gou et al. (2019).

point splicing (Li et al., 2017; Wang et al., 2019a; Iqbal et al., 2021). The primary drawback of this method is that the integrated pore volume distribution curve becomes discontinuous, resulting in significant jumps or clear inflection points at the connection (Fig. 15(b)). This raises concerns about the accuracy of the integrated pore volume distribution. Similar issues may arise with other splicing methods. Overall, full-scale pore and micro-fracture characterization remains a crucial direction in shale reservoir evaluation, and appropriate splicing is essential for this technology. To ensure accuracy, integrated results must be verified with additional analytical test data, such as He-porosity (Zhu et al., 2016; Gou et al., 2019).

5.3. Investigation of pore connectivity

The production of shale gas involves the migration of hydrocarbons from the matrix to hydraulic fractures, a process controlled by the connectivity of μm- and nm-sized pores (Sun et al., 2020b; Gou et al., 2021). Pore connectivity significantly influences the ultimate recovery from shale reservoirs (Hu et al., 2015). Various laboratory techniques, including MICP, spontaneous imbibition, saturated diffusion, SANS, and 3D-CT scanning, have been developed to characterize pore connectivity in shale reservoirs (Clarkson et al., 2013; Yang et al., 2018; Gou et al., 2019; Sun et al., 2020b; Zhao et al., 2020; Zhou et al., 2024b).

MICP was repeated on the same samples to assess pore connectivity by analyzing the residual distribution of mercury across different pore size intervals (Fig. 16(a)). The results show significantly less mercury entering pores smaller than ~13 nm during the second injection. Based on these findings, Sun et al. (2020b) concluded that pores smaller than 13 nm have poor connectivity, suggesting that these pores may serve as storage spaces but exhibit poor flow properties. Additionally, residual mercury was observed in some μm-scale pores, though the cause of this phenomenon remains unclear.

Spontaneous fluid imbibition characteristics are closely linked to the pore connectivity of shale. Deionized (DI) water and *n*-decane are commonly used as intrusion fluids (Hu et al., 2015; Yang et al., 2018; Gao et al., 2019). Pore connectivity is generally categorized into three types: high connectivity (imbibition slope >0.5), intermediate connectivity (slope between 0.26 and 0.5), and poor connectivity (slope <0.26) (Hu et al., 2015; Zhou et al., 2024a). As shown in Fig. 16(b), the slopes decrease as the intrusive fluid migrates from larger to smaller pores, indicating that larger pores have better connectivity (Yang et al., 2018; Gao et al., 2019). Overall, the slopes for *n*-decane are consistently higher than those for DI water, indicating that hydrocarbon-filled pores have greater connectivity. The difference in slopes between the two fluids also reflects differences in pore wettability (Hu et al., 2015; Gao et al., 2019; Zhou et al., 2024a).

Tracer diffusion in brine-saturated shale samples can reflect pore connectivity through the distribution of elements (Fig. 16(c)). There is a positive correlation between element concentration and pore connectivity (Sun et al., 2020b; Zhao et al., 2020). However, the phenomenon of “wall migration” can result in elevated ion concentrations at the sample boundary, potentially leading to misinterpretations (Sun et al., 2020a). While the connectivity assessed by this method provides valuable insights, it lacks quantitative data. Additionally, the interaction between the solution and shales containing high clay content remains unclear, as does the extent of this interaction. These concerns also apply to spontaneous fluid imbibition experiments.

SAS techniques can be used to evaluate pore connectivity by comparing pore size distributions derived from gas intrusion and scattering techniques (Fig. 16(d)). Sun et al. (2020b) obtained pore characteristics from N_2 adsorption and SANS for the same powdered sample (35–80 mesh). In general, gas adsorption is mainly used to evaluate connected pores, while SANS can also characterize isolated pores. In their study, isolated pores were primarily distributed in pore sizes of <2.1 nm and >15 nm (Fig. 16(d)). However, the authors did not provide a clear explanation for the higher N_2 adsorption than SANS in some intervals (Sun et al., 2020b). Despite this, the development of SAS techniques provides a new approach for studying shale pore structure. The scattering technology model used for accessing pore structure still requires further refinement, as it is in its early stages (Clarkson et al., 2013; Sun et al., 2020a).

By combining the He porosity and NMR porosity of saturated hydrogen-bearing fluids in plunger samples, the connected porosity of shale was further investigated through their ratio (Fig. 16(e)) (Gou et al., 2022). In their study, the volume fraction of connected porosity in the Wufeng-Longmaxi shale in the Jiaoshiba area, with a stable tectonic environment, ranged from 69.13% to 94.94% (average 85.12%). However, the distribution intervals for connected or isolated pores were not provided. Furthermore, hydration expansion or hydrogen in the shale (e.g., from organic matter and clay minerals) could introduce errors in the experimental results (Zhang et al., 2018a; Sun et al., 2020a).

Recently, 3D imaging methods have been widely employed to evaluate shale pore connectivity in three-dimensional space (Curtis et al., 2012b; Gou et al., 2019, 2021; Wu et al., 2019, 2020b; Arif et al., 2021; Saraf and Bera, 2021). Several review papers have proposed combining 3D imaging at different scales to describe shale pore and micro-fracture networks at multiple length scales (Ma et al., 2017; Arif et al., 2021; Chandra and Vishal, 2021), which helps address the issue of sample representativeness. This approach holds great potential for exploring dynamic gas adsorption and flow behavior in shale reservoirs (e.g., Yu et al., 2020). However, it is important to consider how to integrate these technologies effectively and the associated financial challenges.

5.4. Description of fractal dimension

Fractal dimension (D) is a reliable petrophysical parameter used to quantify the pore structure and complex surface of irregular porous materials (Mahamud and Novo, 2008; Fu et al., 2022). D varies from 2 to 3, generally increasing with the roughness and inhomogeneity of the pores (Avnir and Jaroniec, 1989; Yao et al., 2008). Several methods, including SEM image analysis (Peng et al., 2017; Li et al., 2018), CT image analysis (Xia et al., 2019), the NMR method (Li et al., 2018), SAS technique (Clarkson et al., 2013; Sun et al., 2020a), MICP method (Lai et al., 2018), thermodynamic method (Fu et al., 2022), BET model (Avnir and Jaroniec, 1989; Fu et al., 2022), and the Frenkel-Halsey-Hill (FHH) equation (Yao et al., 2008; Gou et al., 2023), have been proposed to calculate fractal dimension. Among these, the FHH equation based on gas adsorption is proven to be one of the most effective and is the most commonly used method (Avnir and Jaroniec, 1989). The FHH equation is described as follows:

$$\ln(V) = K \times [\ln(\ln(P_0 / P))] + \text{Constant} \quad (2)$$

where V is the adsorption volume, cm^3/g; P_0 is the vapor saturation pressure, MPa; P is the equilibrium pressure, MPa; and K is the slope of plot between $\ln(V)$ and $\ln(\ln(P_0/P))$. It is worth noting that there are generally two explanations for D: '$K = (D-3)/3$' and '$K = (D-3)$' (Pyun and Rhee, 2004). However, the work of Yao et al. (2008) suggests that the equation of '$K = (D-3)$' provides more realistic results.

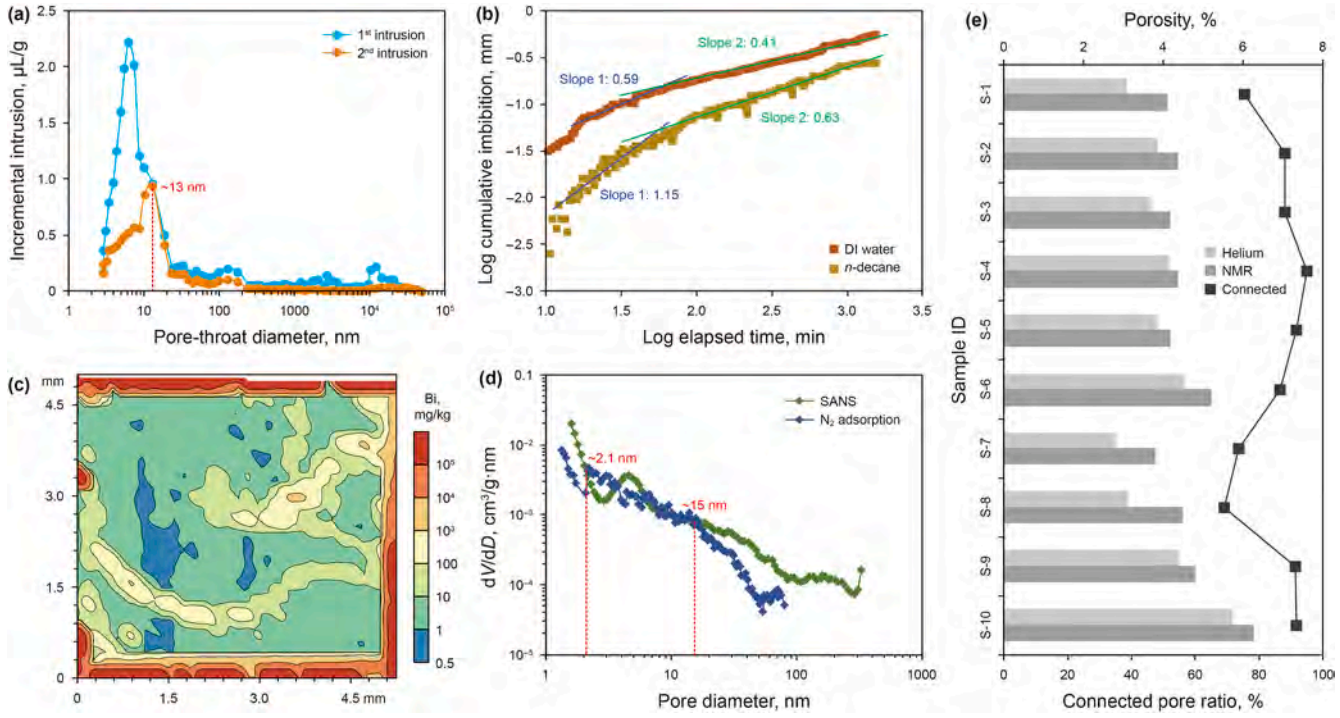

Fig. 16. Characterization of pore connectivity in shale reservoirs using different methods: **(a)** illustrates the determination of connected pores through repeated mercury intrusion experiments on the same sample, based on differences in pore size distribution, modified from Sun et al. (2020b); **(b)** employs the fluid imbibition method to assess pore connectivity; a slope greater than 0.5 indicates good connectivity, modified from Yang et al. (2018); **(c)** evaluates pore connectivity via tracer diffusion, where higher ion concentration correlates with better connectivity, modified from Zhao et al. (2020); **(d)** uses SANS and N_2 adsorption to assess pore connectivity. SANS characterizes both connected and isolated pores, while N_2 adsorption measures only connected pores, and the difference between the two reveals the location of isolated pores, modified from Sun et al. (2020a); **(e)** assesses connectivity using the ratio of He-porosity to NMR porosity, where the ratio represents the proportion of connected pores, modified from Gou et al. (2022).

The ongoing debate surrounding the use of the two-phase method (Yao et al., 2008; Fu et al., 2022) versus the three-phase method (Peng et al., 2017; Feng et al., 2020) for calculating fractal dimension (D) using the FHH equation continues to attract attention. The two-phase method uses a relative pressure (P/P_0) threshold of ~0.45, dividing the N_2 adsorption isotherm into two sections: a low-pressure section ($P/P_0 < 0.45$) and a high-pressure section ($P/P_0 > 0.45$) (Fig. 17(a)–(c)). The fractal dimension (D_1) of the low-pressure section reflects pore surface roughness and is primarily influenced by van der Waals forces (Fu et al., 2022). In

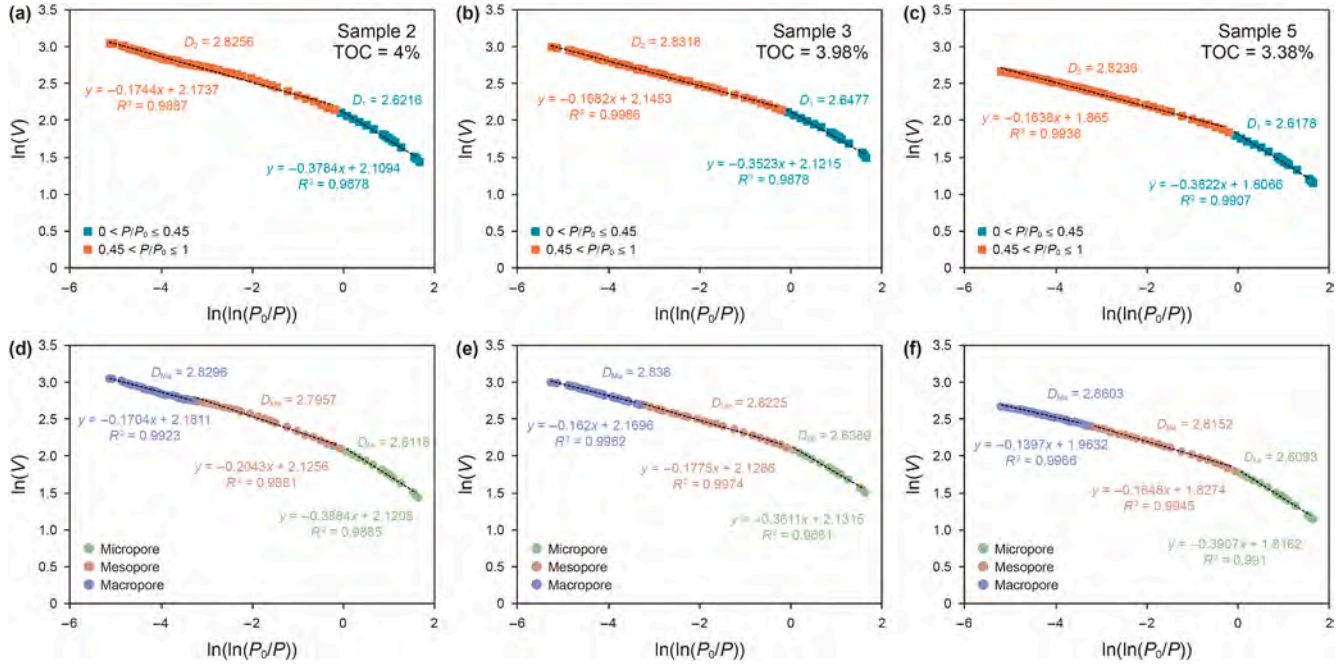

Fig. 17. Comparison of the fractal dimension results calculated by the two-phase and three-phase methods from N_2 adsorption isotherms. Gas adsorption data are modified from Xu et al. (2020a).

contrast, the fractal dimension (D_2) of the high-pressure section is closely associated with pore arrangement and connectivity, representing capillary condensation processes (Yao et al., 2008). The three-phase method, based on the Kelvin equation, divides N_2 adsorption into three stages: micropore, mesopore, and macropore adsorption, with corresponding relative pressures of <0.4, 0.4–0.96, and >0.96, respectively (Fig. 17(d)–(f)) (Peng et al., 2017; Feng et al., 2020).

As illustrated in Fig. 17, each segment in both the two-phase and three-phase methods demonstrates a strong linear relationship, with correlation coefficients exceeding 0.98. The calculated D values fall within the defined interval, indicating that both methods effectively calculate the fractal dimension. However, as mentioned earlier, there is an optimal characterization range for gas adsorption (Clarkson et al., 2013; Anovitz and Cole, 2015). The N_2 adsorption technique is best suited for investigating pores in the 2–300 nm

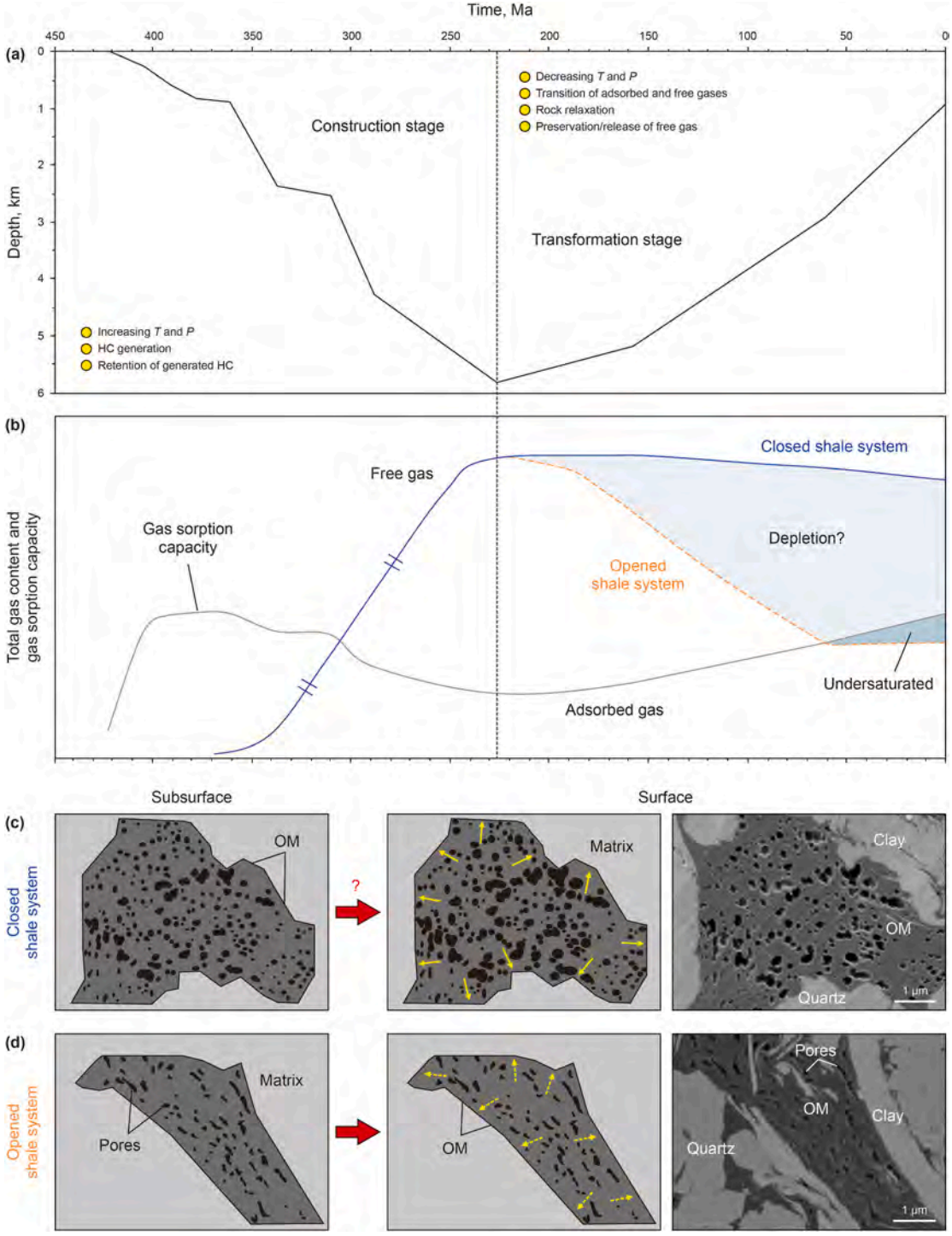

Fig. 18. Schematic diagram showing the evolution of gas contents during burial and uplift stages **(a)–(b)**, and the possible variation of pore structure from present-day burial to the surface with various shale systems **(c)–(d)**. **(a)** and **(b)** are modified from Hao et al. (2013). A solid yellow arrow indicates a stronger pore expansion effect, while a dashed arrow represents a weaker pore expansion effect. T = temperature; P = pressure; HC = hydrocarbons.

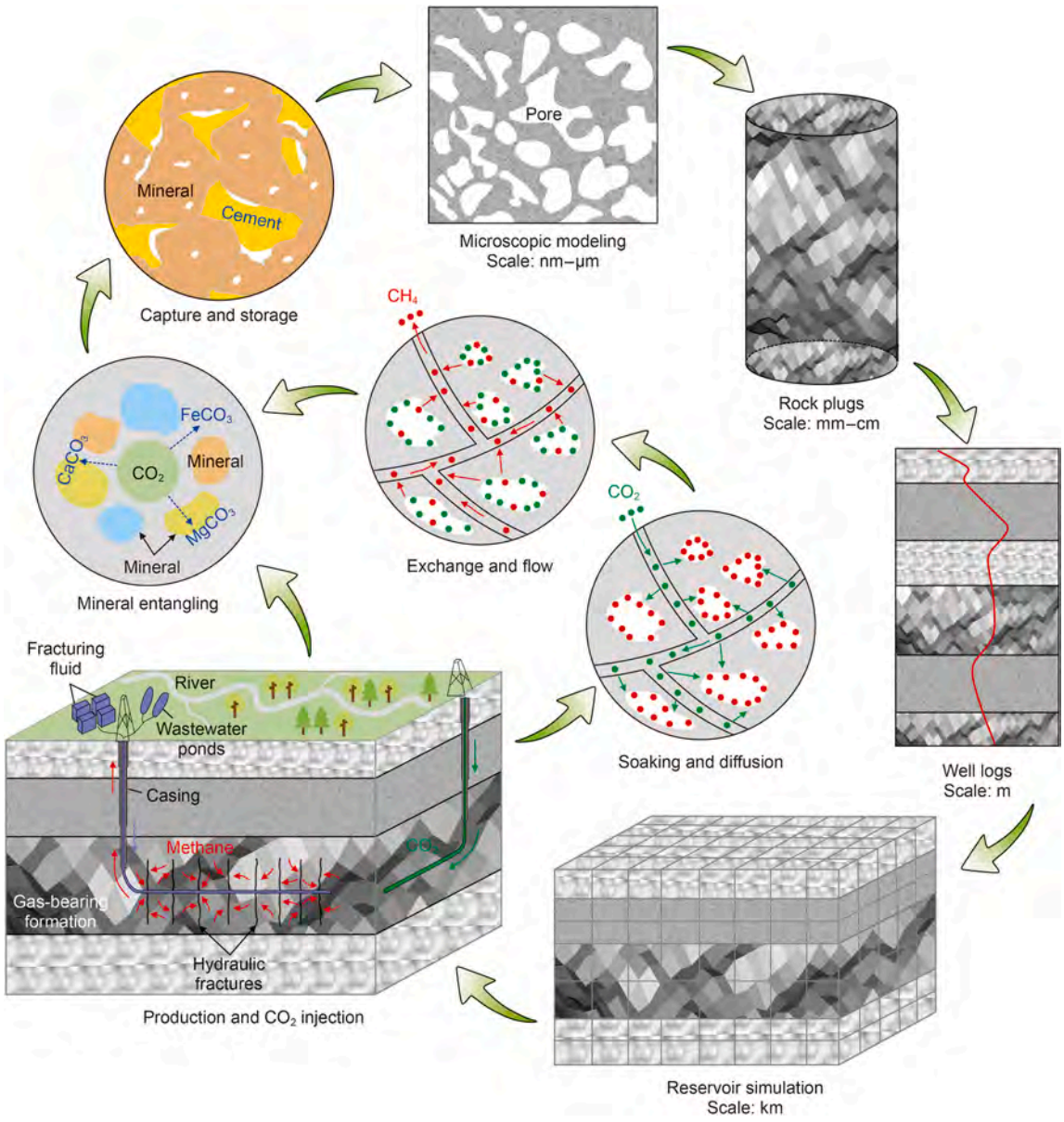

Fig. 19. The concept of circulation from pore characterization to shale gas production and development, as well as carbon sequestration.

range (Anovitz and Cole, 2015; Ma et al., 2017). Thus, data outside this range should be excluded to minimize potential experimental errors. The two-phase method, unfortunately, does not account for this limitation (Yao et al., 2008). While the three-phase method shares similar constraints, the middle segment ($P/P_0 = 0.4$–0.96) is entirely within the optimal characterization range. Moreover, the pores within this segment are predominantly subject to capillary condensation, which is the primary focus of the FHH model (Fu et al., 2022). Therefore, it is reasonable to suggest that the three-phase method may be more suitable for calculating fractal dimension using gas adsorption techniques. At the very least, the calculated values for mesopores are accurate and reliable.

5.5. Are the observed porous spaces genuine

After reviewing the prospects and challenges of shale pore characterization, the critical question we must address is whether the pore space observed in the laboratory accurately reflects that under the original formation conditions. Generally, high- and over-mature shales at present-day depths, suitable for commercial gas production, undergo two stages: deep burial and uplift (Fig. 18(a)). The deep burial stage is typically associated with pressurization from hydrocarbon generation, while the uplift stage is linked to pressure loss (Fig. 18(a) and (b)) (Hao et al., 2013; He et al., 2020; Gou et al., 2025). In a closed shale system, the pore pressure loss during the uplift stage is minimal, leading to overpressure at present-day depths (Hao et al., 2013; Xu et al., 2020a, 2020b). In other words, the loss of pore pressure is likely smaller than the reduction in overburden rock pressure caused by formation erosion. As a result, pore volume tends to increase during uplift and erosion due to gas expansion, particularly under conditions of high residual hydrocarbons (Yu and Sepehrnoori, 2014). For example, Xia et al. (2020) conducted numerical simulations using pressure-volume-temperature

(PVT) coupling and fluid dynamics calculations, showing that due to the uplift of the strata from 4000 m to 2000 m, porosity could increase from 6% to 6.6%. However, laboratory samples are typically sourced from depths greater than 2000 m (Sanei and Ardakani, 2016; İnan et al., 2018; Gou et al., 2019, 2021, 2025; Xu et al., 2020a, 2020c) and lack the pressure constraints imposed by the overlying strata. This raises concerns about the reliability of pore structure measurements in overpressure systems under experimental conditions.

While it is evident that closed shale systems exhibit superior storage capacity and regular pore morphology under formation conditions (Hao et al., 2013; Gou et al., 2021), the degree of change in pore structure when shale is brought to the surface remains a significant issue (Fig. 18(c)) (Xia et al., 2020). A common approach to simulate pore structures under formation conditions is to heat shale samples under confining pressure and evaluate the final pore structure (Gao et al., 2020; Shao et al., 2022). However, two challenges persist: (1) the temperature and pressure of experimental conditions are difficult to match with those under formation conditions, and (2) during testing, both the temperature and pressure fields are removed, so the conditions no longer reflect in-situ formation conditions. Pressure retention coring offers another potential solution to address pore expansion effects (Pinkett and Westacott, 2016; Zhao et al., 2023b). After the sample is extracted under pressure retention, it should be rapidly frozen to prevent hydrocarbon loss or pore expansion due to temperature and pressure changes. Sample preparation and observation should follow immediately after the freezing process. If conditions allow, these procedures could be completed at low temperatures, ensuring the observed pores reflect the characteristics under original formation conditions. However, the cost and complexity of pressure retention coring and freezing treatment pose significant barriers to widespread adoption.

Conversely, in an open fluid system, a significant amount of shale gas is lost during the uplift phase (Hao et al., 2013; Xu et al., 2020a, 2020b; Gou et al., 2025). In such systems, shale typically exhibits underpressure or normal pressure at present-day depths (He et al., 2020). Without the support from overpressure mechanisms, pores are generally compressed or even closed by the pressure exerted by overburden strata (Gou et al., 2021). Consequently, even when these shales are brought to the surface, pore structures do not undergo significant changes in the absence of gas expansion (Fig. 18(d)). Therefore, the effect of pore variation should be carefully considered in South China, given the wide pressure range caused by complex tectonic settings following the cessation of hydrocarbon generation (Hao et al., 2013; He et al., 2020; Gou et al., 2025).

The mechanisms of pore space expansion and alteration are discussed, with the presence of micro-fractures in deep strata—observed in samples—remaining a topic of considerable debate. Recovering shales from depth can induce stress-relief micro-fractures due to decompression and gas exsolution from pore fluids (Gale et al., 2007; Clarkson et al., 2016). These stress-relief micro-fractures, commonly observed in SEM images, are an inevitable consequence of core recovery from depth (Meng et al., 2021). They are typically parallel to the laminations and the orientation of clay particles. However, some studies suggest that micro-fractures appearing to interconnect larger pores within the bedding plane may have a natural origin (Ougier-Simonin et al., 2016). These micro-fractures may also indicate the presence of hydrocarbons (Clarkson et al., 2016; Xu et al., 2020b). Overall, accurately quantifying the micro-fractures that remain absent or are only slightly opened under in-situ conditions is a significant challenge. A careful analysis of fracture wall morphology may only provide a provisional and qualitative answer.

6. Conclusions and outlook for future research

Shale reservoirs are characterized by complex and heterogeneous pore structures, which significantly impact fluid flow, gas storage capacity, and enrichment levels. Although significant progress has been made in experimental techniques, several critical issues persist, hindering the precise quantification of pore characteristics. One of the primary challenges in pore feature analysis lies in sample preparation. Methods such as SEM and gas adsorption are widely used and regarded as reliable; however, factors such as sample size, preparation procedures, and experimental conditions—including voltage and current settings—can introduce variability, affecting the accuracy of results. Furthermore, integrating multiple techniques remains a significant challenge. While combining methods like SEM, gas adsorption, and CT scanning can provide a more comprehensive understanding of the pore system, discrepancies in experimental settings and analysis techniques can complicate data integration. For shale reservoir characterization research, two key points emerge. First, progress must be made in standardizing sample preparation to address inconsistencies in experimental conditions. Improving sample size determination and preparation protocols for methods like gas adsorption and SEM will reduce errors and enhance the accuracy of pore characterization. Second, new experimental methods should aim to overcome current limitations by increasing the sensitivity and resolution of pore structure characterization. Emerging technologies such as nano-CT, micro-CT, and related methods hold the potential to provide more precise, three-dimensional visualizations of pore systems at different scales. Additionally, future research should focus on the following directions:

1) **Upscaling the representativeness of results at larger scales.** To effectively model and present petrophysical properties at the macro scale, reliable pore-scale data must be upscaled. However, ultra-high-resolution technologies may reduce sample representativeness at larger scales. Thus, adopting complementary technical methods is crucial. Microscopic data should be integrated and expanded to macro scales, correlating nanoscale and centimeter-scale microstructures with well-log or seismic datasets to enhance reservoir predictions (Fig. 19). Nevertheless, the integration of various technologies should be handled carefully.
2) **Developing and enabling advanced techniques.** Improvements in 3D imaging technologies are crucial for capturing pore space heterogeneity and improving reservoir predictions, but they remain static. We anticipate that 4D scanning (3D plus time) will become a standard tool in reservoir characterization. This technology has the potential to track pore evolution, fluid migration, and hydrocarbon production in shale reservoirs. Advances in techniques like SAS and NMR will contribute to this development.
3) **Entering deep reservoirs and enhancing micro-fracture evaluation.** Deep shale gas reservoirs (buried depths >3500 m) are increasingly recognized as a key resource for future exploration. However, the intense diagenesis at such depths complicates pore structure prediction and the assessment of physical properties. Greater attention should be given to the storage and flow behavior of micro-fractures, especially considering the brittle-to-plastic transformation in deep shale gas. Research on the synergistic integration of geological and engineering factors is needed.
4) **Expanding carbon capture and storage.** The integration of carbon capture and storage with pore characterization is vital for optimizing CO_2 sequestration and gas recovery in shale

reservoirs. CO_2 injection competes with methane for adsorption, promoting methane desorption and enhancing gas production (Heller and Zoback, 2014; Bacon et al., 2015; Li et al., 2024). CO_2 also reacts with the rock to form stable minerals (Wei et al., 2023), improving sequestration at the microscopic scale (Fig. 19). Real-time monitoring of pore changes is crucial for optimizing CO_2 injection strategies and enhancing shale gas production. Accurate evaluation of pore structure and sequestration forms an integrated framework, representing a key direction for future research.

CRediT authorship contribution statement

Qi-Yang Gou: Writing – original draft, Investigation, Conceptualization. **Shang Xu:** Validation, Supervision. **Fang Hao:** Formal analysis, Funding acquisition. **Ke-Yu Liu:** Writing – review & editing, Validation. **Zhang-Xing Chen:** Supervision, Formal analysis.

Conflict of interest

We declare that we have no financial and personal relationships with other people or organizations that can inappropriately influence our work, there is no professional or other personal interest of any nature or kind in any product, service and/or company that could be construed as influencing the position presented in the manuscript entitled.

Acknowledgements

This research was supported by the Postdoctoral Fellowship Program of CPSF (GZC20250291), the Scientific Research Innovation Capability Support Project for Young Faculty (SRICSPYF-BS2025032), the National Natural Science Foundation of China (U24B6002, U25D9024, 42488101), the Key R&D Program of Shandong Province, China (2024CXPT076), China Postdoctoral Science Foundation (2025M780451), Shandong Postdoctoral Science Foundation (SDBX2024010), and the Independent Innovation Research Program of China University of Petroleum (East China) (24CX06084A).

References

Abolghasemi, E., Andersen, P.Ø., 2022. The influence of adsorption layer thickness and pore geometry on gas production from tight compressible shales. Adv. Geo-Energy Res. 6 (1), 4–22. https://doi.org/10.46690/ager.2022.01.02.

Afagwu, C., Mahmoud, M.A., Alafnan, S., et al., 2022. Multiscale storage and transport modeling in unconventional shale gas: A review. J. Petrol. Sci. Eng. 208, 109518. https://doi.org/10.1016/j.petrol.2021.109518.

Anovitz, L.M., Cole, D.R., 2015. Characterization and analysis of porosity and pore structures. Rev. Mineral. Geochem. 80 (1), 61–164. https://doi.org/10.2138/rmg.2015.80.04.

Anovitz, L.M., Cole, D.R., Rother, G., et al., 2013. Diagenetic changes in macro- to nano-scale porosity in the St. Peter Sandstone: An (ultra) small angle neutron scattering and backscattered electron imaging analysis. Geochem. Cosmochim. Acta 102, 280–305. https://doi.org/10.1016/j.gca.2012.07.035.

Arif, M., Mahmoud, M., Zhang, Y., et al., 2021. X-ray tomography imaging of shale microstructures: A review in the context of multiscale correlative imaging. Int. J. Coal Geol. 233, 103641. https://doi.org/10.1016/j.coal.2020.103641.

Avnir, D., Jaroniec, M., 1989. An isotherm equation for adsorption on fractal surfaces of heterogeneous porous materials. Langmuir 5 (6), 1431–1433. https://doi.org/10.1021/la00090a032.

Bacon, D.H., Yonkofski, C.M.R., Schaef, H.T., et al., 2015. CO_2 storage by sorption on organic matter and clay in gas shale. J. Unconv. Oil Gas Resour. 12, 123–133. https://doi.org/10.1016/j.juogr.2015.09.004.

Bai, L.H., Liu, B., Xie, Z.H., 2023. A novel method for evaluating the shale oil movability in laboratory by using high-field NMR and sequential extraction. In: Proceedings of the 11th Unconventional Resources Technology Conference. American Association of Petroleum Geologists, pp. 2812–2822. https://doi.org/10.15530/urtec-2023-3860713.

Bera, A., Shah, S., 2021. A review on modern imaging techniques for characterizati on of nanoporous unconventional reservoirs: Challenges and prospects. Mar. Petrol. Geol. 133, 105287. https://doi.org/10.1016/j.marpetgeo.2021.105287.

Bernard, S., Brown, L., Wirth, R., et al., 2013. FIB-SEM and TEM investigations of an organic-rich shale maturation series from the lower Toarcian Posidonia Shale, Germany: Nanoscale pore system and fluid-rock interactions. In: Camp, W.K., Diaz, E., Wawak, B. (Eds.), Electron Microscopy of Shale Hydrocarbon Reservoirs. AAPG Memoir, vol. 102, pp. 53–66. https://doi.org/10.1306/13391705M1023583.

Bernard, S., Wirth, R., Schreiber, A., et al., 2012. Formation of nanoporous pyrobitumen residues during maturation of the Barnett Shale (Fort Worth Basin). Int. J. Coal Geol. 103, 3–11. https://doi.org/10.1016/j.coal.2012.04.010.

Bertier, P., Schweinar, K., Stanjek, H., et al., 2016. On the use and abuse of N_2 physisorption for the characterization of the pore structure of shales. In: Schäfer, T., Dohrmann, R., Greenwell, H.C. (Eds.), Filling the Gaps – from Microscopic Pore Structures to Transport Properties in Shales, Clay Minerals Society Workshop Lectures, vol. 21, pp. 151–161. https://doi.org/10.1346/CMS-WLS-21-12.

Blach, T., Radlinski, A.P., Vu, P., et al., 2021. Deformation of pores in response to uniaxial and hydrostatic stress cycling in Marcellus Shale: Implications for gas recovery. Int. J. Coal Geol. 248, 103867. https://doi.org/10.1016/j.coal.2021.103867.

Buades, A., Coll, B., Morel, J.M., 2006. Image and movie denoising by nonlocal means. Int. J. Comput. Vis. 76 (2), 1–25. https://doi.org/10.1007/s11263-007-0052-1.

Bultreys, T., De Boever, W., Cnudde, V., 2016. Imaging and image-based fluid transport modeling at the pore scale in geological materials: A practical introduction to the current state-of-the-art. Earth Sci. Rev. 155, 93–128. https://doi.org/10.1016/j.earscirev.2016.02.001.

Cai, J.C., Jiao, X.H., Wang, H., et al., 2024. Multiphase fluid-rock interactions and flow behaviors in shale nanopores: A comprehensive review. Earth Sci. Rev. 257, 104884. https://doi.org/10.1016/j.earscirev.2024.104884.

Cao, T.T., Song, Z.G., Liu, G.X., et al., 2016. Characteristics of shale pores, fractal dimension and their controlling factors determined by nitrogen adsorption and mercury injection methods. Petrol. Geol. Recovery Effic. 23 (2), 1–8. https://doi.org/10.13673/j.cnki.cn37-1359/te.20151215.002 (in Chinese).

Chalmers, G.R., Bustin, R.M., Power, I.M., 2012. Characterization of gas shale pore systems by porosimetry, pycnometry, surface area, and field emission scanning electron microscopy/transmission electron microscopy image analyses: Examples from the Barnett, Woodford, Haynesville, Marcellus, and Doig units. AAPG Bull. 96 (6), 1099–1119. https://doi.org/10.1306/10171111052.

Chandra, D., Vishal, V., 2021. A critical review on pore to continuum scale imaging techniques for enhanced shale gas recovery. Earth Sci. Rev. 217, 103638. https://doi.org/10.1016/j.earscirev.2021.103638.

Chandra, D., Vishal, V., Bahadur, J., et al., 2020. A novel approach to identify accessible and inaccessible pores in gas shales using combined low-pressure sorption and SAXS/SANS analysis. Int. J. Coal Geol. 228, 103556. https://doi.org/10.1016/j.coal.2020.103556.

Chen, S.W., Pellequer, J.L., 2011. DeStripe: Frequency-based algorithm for removing stripe noises from AFM images. BMC Struct. Biol. 11, 7. https://doi.org/10.1186/1472-6807-11-7.

Chen, Y.Y., Wei, L., Mastalerz, M., et al., 2015. The effect of analytical particle size on gas adsorption porosimetry of shale. Int. J. Coal Geol. 138, 103–112. https://doi.org/10.1016/j.coal.2014.12.012.

Chen, Z.Y., Song, Y., Jiang, Z.X., et al., 2019. Identification of organic matter components and organic pore characteristics of marine shale: A case study of Wufeng-Longmaxi shale in southern Sichuan Basin, China. Mar. Petrol. Geol. 109, 56–69. https://doi.org/10.1016/j.marpetgeo.2019.06.002.

Clarkson, C.R., Haghshenas, B., Ghanizadeh, A., et al., 2016. Nanopores to megafractures: Current challenges and methods for shale gas reservoir and hydraulic fracture characterization. J. Nat. Gas Sci. Eng. 31, 612–657. https://doi.org/10.1016/j.jngse.2016.01.041.

Clarkson, C.R., Solano, N., Bustin, R.M., et al., 2013. Pore structure characterization of North American shale gas reservoirs using USANS/SANS, gas adsorption, and mercury intrusion. Fuel 103, 606–616. https://doi.org/10.1016/j.fuel.2012.06.119.

Curtis, M.E., 2010. Structural characterization of gas shales on the micro- and nano-scales. In: Canadian Unconventional Resources and International Petroleum Conference. https://doi.org/10.2118/137693-MS.

Curtis, M.E., Cardott, B.J., Sondergeld, C.H., et al., 2012a. Development of organic porosity in the Woodford Shale with increasing thermal maturity. Int. J. Coal Geol. 103, 26–31. https://doi.org/10.1016/j.coal.2012.08.004.

Curtis, M.E., Sondergeld, C.H., Ambrose, R.J., et al., 2012b. Microstructural investigation of gas shales in two and three dimensions using nanometer-scale resolution imaging. AAPG Bull. 96 (4), 665–677. https://doi.org/10.1306/08151110188.

Dong, T., Harris, N.B., 2020. The effect of thermal maturity on porosity development in the Upper Devonian–Lower Mississippian Woodford Shale, Permian Basin, US: Insights into the role of silica nanospheres and microcrystalline quartz on porosity preservation. Int. J. Coal Geol. 217, 103346. https://doi.org/10.1016/j.coal.2019.103346.

Fan, Y.C., Liu, K.Y., Pu, X.G., et al., 2022. Morphological classification and three-dimensional pore structure reconstruction of shale oil reservoirs: A case from the second member of Paleogene Kongdian Formation in the Cangdong Sag,

Bohai Bay Basin, East China. Petrol. Explor. Dev. 49 (5), 1085–1097. https://doi.org/10.1016/S1876-3804(22)60334-3.
Feng, W.P., Wang, F.Y., Guan, J., et al., 2018. Geologic structure controls on initial productions of lower Silurian Longmaxi shale in South China. Mar. Petrol. Geol. 91, 163–178. https://doi.org/10.1016/j.marpetgeo.2018.01.001.
Feng, Z.Q., Hao, F., Zhou, S.W., et al., 2020. Pore systems of the different lithofacies of the Longmaxi Formation at depths exceeding 3500 m in the Zigong area, Sichuan Basin. Energy Fuels 34 (5), 5733–5752. https://doi.org/10.1021/acs.energyfuels.0c00456.
Fitschen, J.H., Ma, J., Schuff, S., 2017. Removal of curtaining effects by a variational model with directional forward differences. Comput. Vis. Image Underst. 155, 24–32. https://doi.org/10.1016/j.cviu.2016.12.008.
Fu, H.J., Yan, D.T., Yao, C.P., et al., 2022. Pore structure and multi-scale fractal characteristics of adsorbed pores in marine shale: A case study of the lower Silurian Longmaxi Shale in the Sichuan Basin, China. J. Earth Sci. 33 (5), 1278–1290. https://doi.org/10.1007/s12583-021-1602-0.
Gale, J.F.W., Reed, R.M., Holder, J., 2007. Natural fractures in the Barnett Shale and their importance for hydraulic fracture treatments. AAPG Bull. 91 (4), 603–622. https://doi.org/10.1306/11010606061.
Gannaway, G., 2014. NMR investigation of pore structure in gas shales. SPE Annual Technical Conference and Exhibition, Amsterdam, The Netherlands, October 2014, paper number: SPE-173474-STU. https://doi.org/10.2118/173474-STU.
Gao, Z.Y., Fan, Y.P., Hu, Q.H., et al., 2019. A review of shale wettability characterization using spontaneous imbibition experiments. Mar. Petrol. Geol. 109, 330–338. https://doi.org/10.1016/j.marpetgeo.2019.06.035.
Gao, Z.Y., Fan, Y.P., Xuan, Q.X., et al., 2020. A review of shale pore structure evolution characteristics with increasing thermal maturities. Adv. Geo-Energy Res. 4 (3), 247–259. https://doi.org/10.46690/ager.2020.03.03.
Giesche, H., 2006. Mercury porosimetry: A general (practical) overview. Part. Part. Syst. Char. 23 (1), 9–19. https://doi.org/10.1002/ppsc.200601009.
Gou, Q.Y., Hao, Y.X., Xu, S., et al., 2025. Controls of shale gas enrichment and high yield in the Lower Cambrian Niutitang shale of the Yichang area, southern China. AAPG Bull. 109 (11), 1379–1402. https://doi.org/10.1306/08192524086.
Gou, Q.Y., Xu, S., 2019. Quantitative evaluation of free gas and adsorbed gas content of Wufeng-Longmaxi shales in the Jiaoshiba area, Sichuan Basin, China. Adv. Geo-Energ. Res. 3 (3), 258–267. https://doi.org/10.26804/ager.2019.03.04.
Gou, Q.Y., Xu, S., Chen, Z.X., et al., 2023. Novel method for the classification of shale oil reservoirs associated with mobility: Inspiration from gas adsorption and multiple isothermal stage pyrolysis. Energy Fuel. 37 (13), 9121–9130. https://doi.org/10.1021/acs.energyfuels.3c01172.
Gou, Q.Y., Xu, S., Hao, F., et al., 2019. Full-scale pores and micro-fractures characterization using FE-SEM, gas adsorption, nano-CT and micro-CT: A case study of the Silurian Longmaxi Formation shale in the Fuling area, Sichuan Basin, China. Fuel 253, 167–179. https://doi.org/10.1016/j.fuel.2019.04.116.
Gou, Q.Y., Xu, S., Hao, F., et al., 2020. Quantitative calculated shale gas contents with different lithofacies: A case study of Fuling gas shale, Sichuan Basin, China. J. Nat. Gas Sci. Eng. 76. https://doi.org/10.1016/j.jngse.2020.103222.
Gou, Q.Y., Xu, S., Hao, F., et al., 2021. The effect of tectonic deformation and preservation condition on the shale pore structure using adsorption-based textural quantification and 3D image observation. Energy 219, 119579. https://doi.org/10.1016/j.energy.2020.119579.
Gou, Q.Y., Xu, S., Hao, F., et al., 2022. Evaluation of shale pore connectivity and effectiveness in the Jiaoshiba area, Sichuan Basin. Acta Sedimentol. Sin. 40 (5), 1419–1426. https://doi.org/10.14027/j.issn.1000-0550.2021.067 (in Chinese).
Grobe, A., Schmatz, J., Littke, R., et al., 2017. Enhanced surface flatness of vitrinite particles by broad ion beam polishing and implications for reflectance measurements. Int. J. Coal Geol. 180, 113–121. https://doi.org/10.1016/j.coal.2017.05.006.
Groen, J.C., Peffer, L.A.A., Pérez-Ramıírez, J., 2003. Pore size determination in modified micro- and mesoporous materials. Pitfalls and limitations in gas adsorption data analysis. Microporous Mesoporous Mater. 60 (1–3), 1–17. https://doi.org/10.1016/S1387-1811(03)00339-1.
Han, H., Cao, Y., Chen, S.J., et al., 2016. Influence of particle size on gas-adsorption experiments of shales: An example from a Longmaxi Shale sample from the Sichuan Basin, China. Fuel 186, 750–757. https://doi.org/10.1016/j.fuel.2016.09.018.
Han, H., Pang, P., Li, Z.L., et al., 2019. Controls of organic and inorganic compositions on pore structure of lacustrine shales of Chang 7 member from Triassic Yanchang Formation in the Ordos Basin. China. Mar. Petrol. Geol. 100, 270–284. https://doi.org/10.1016/j.marpetgeo.2018.10.038.
Hao, F., Zou, H.Y., 2013. Cause of shale gas geochemical anomalies and mechanisms for gas enrichment and depletion in high-maturity shales. Mar. Petrol. Geol. 44, 1–12. https://doi.org/10.1016/j.marpetgeo.2013.03.005.
Hao, F., Zou, H.Y., Lu, Y.C., 2013. Mechanisms of shale gas storage: Implications for shale gas exploration in China. AAPG Bull. 97 (8), 1325–1346. https://doi.org/10.1306/02141312091.
Hazra, B., Wood, D.A., Vishal, V., et al., 2018. Pore characteristics of distinct thermally mature shales: Influence of particle size on low-pressure CO_2 and N_2 adsorption. Energy Fuels 32 (8), 8175–8186. https://doi.org/10.1021/acs.energyfuels.8b01439.
He, Q., Dong, T., Hu, D.F., et al., 2021. The influence of analytical particle size on the pore system measured by CO_2, N_2, and Ar adsorption experiments for shales. Energy Fuel. 35 (22), 18637–18652. https://doi.org/10.1021/acs.energyfuels.1c02897.
He, Z.L., Nie, H.K., Li, S.J., et al., 2020. Differential enrichment of shale gas in upper Ordovician and lower Silurian controlled by the plate tectonics of the Middle-Upper Yangtze, South China. Mar. Petrol. Geol. 118, 104357. https://doi.org/10.1016/j.marpetgeo.2020.104357.
Heller, R., Zoback, M., 2014. Adsorption of methane and carbon dioxide on gas shale and pure mineral samples. J. Unconv. Oil Gas Resour. 8, 14–24. https://doi.org/10.1016/j.juogr.2014.06.001.
Hu, Q.H., Ewing, R.P., Rowe, H.D., 2015. Low nanopore connectivity limits gas production in Barnett formation. J. Geophys. Res. Solid Earth 120 (12), 8073–8087. https://doi.org/10.1002/2015JB012103.
Hua, J.J., Liu, Z.W., Lin, C.C., et al., 2014. Investigation on charging for field emission scanning electron microscope. J. Chin. Electron Microsc. Soc. 33 (3), 226–232. https://doi.org/10.3969/j.1000-6281.2014.03.006 (in Chinese).
Ilavsky, J., Jemian, P.R., 2009. Irena: Tool suite for modeling and analysis of small-angle scattering. J. Appl. Crystallogr. 42 (2), 347–353. https://doi.org/10.1107/S0021889809002222.
Imbraguglio, D., Giovannozzi, A.M., Nastro, A., et al., 2012. Submicron machining and biomolecule immobilization on porous silicon by electron beam. Nanoscale Res. Lett. 7, 530. https://doi.org/10.1186/1556-276X-7-530.
İnan, S., Al Badairy, H., İnan, T., et al., 2018. Formation and occurrence of organic matter-hosted porosity in shales. Int. J. Coal Geol. 199, 39–51. https://doi.org/10.1016/j.coal.2018.09.021.
Iqbal, M.A., Rezaee, R., Smith, G., et al., 2021. Shale lithofacies controls on porosity and pore structure: An example from Ordovician Goldwyer Formation, Canning Basin, Western Australia. J. Nat. Gas Sci. Eng. 89, 103888. https://doi.org/10.1016/j.jngse.2021.103888.
Jiang, F.J., Huo, L.N., Chen, D., et al., 2023. The controlling factors and prediction model of pore structure in global shale sediments based on random forest machine learning. Earth Sci. Rev. 241, 104442. https://doi.org/10.1016/j.earscirev.2023.104442.
Jiang, Z.X., Tang, X.L., Li, Z., et al., 2016. The whole-aperture pore structure characteristics and its effect on gas content of the Longmaxi Formation shale in the southeastern Sichuan Basin. Earth Sci. Front. 23 (2), 126–134. https://doi.org/10.13745/j.esf.2016.02.013 (in Chinese).
Jiao, L., Andersen, P.Ø., Zhou, J.P., et al., 2020. Applications of mercury intrusion capillary pressure for pore structures: A review. Capillarity 3 (4), 62–74. https://doi.org/10.46690/capi.2020.04.02.
Jin, Z.J., Zhu, R.K., Liang, X.P., et al., 2021. Several issues worthy of attention in current lacustrine shale oil exploration and development. Petrol. Explor. Dev. 48 (6), 1471–1484. https://doi.org/10.1016/S1876-3804(21)60303-8.
Juenger, M.C.G., Jennings, H.M., 2001. The use of nitrogen adsorption to assess the microstructure of cement paste. Cement Concr. Res. 31 (6), 883–892. https://doi.org/10.1016/S0008-8846(01)00493-8.
Katz, A.J., Thompson, A.H., 1986. Quantitative prediction of permeability in porous rock. Phys. Rev. B 34 (11), 8179–8181. https://doi.org/10.1103/PhysRevB.34.8179.
Katz, B.J., Arango, I., 2018. Organic porosity: A geochemist's view of the current state of understanding. Org. Geochem. 123, 1–16. https://doi.org/10.1016/j.orggeochem.2018.05.015.
Klaver, J., Desbois, G., Urai, J.L., et al., 2012. BIB-SEM study of the pore space morphology in early mature Posidonia Shale from the Hils area, Germany. Int. J. Coal Geol. 103, 12–25. https://doi.org/10.1016/j.coal.2012.06.012.
Kuila, U., McCarty, D.K., Derkowski, A., et al., 2014. Total porosity measurement in gas shales by the water immersion porosimetry (WIP) method. Fuel 117, 1115–1129. https://doi.org/10.1016/j.fuel.2013.09.073.
Kuila, U., Prasad, M., 2013. Specific surface area and pore-size distribution in clays and shales. Geophys. Prospect. 61 (2), 341–362. https://doi.org/10.1111/1365-2478.12028.
Kwiecińska, B., Pusz, S., Valentine, B.J., 2019. Application of electron microscopy TEM and SEM for analysis of coals, organic-rich shales and carbonaceous matter. Int. J. Coal Geol. 211, 103203. https://doi.org/10.1016/j.coal.2019.05.010.
Kwon, O., Kronenberg, A.K., Gangi, A.F., et al., 2004. Permeability of illite-bearing shale: 1. Anisotropy and effects of clay content and loading. J. Geophys. Res. 109 (B10), 2004JB003052. https://doi.org/10.1029/2004jb003052.
Lai, J., Wang, G.W., Wang, Z.Y., et al., 2018. A review on pore structure characterization in tight sandstones. Earth Sci. Rev. 177, 436–457. https://doi.org/10.1016/j.earscirev.2017.12.003.
Lee, S., Fischer, T.B., Stokes, M.R., et al., 2014. Dehydration effect on the pore size, porosity, and fractal parameters of shale rocks: Ultrasmall-angle X-ray scattering study. Energy Fuel. 28 (11), 6772–6779. https://doi.org/10.1021/ef501427d.
Lei, J., Pan, B.Z., Guo, Y.H., et al., 2021. A comprehensive analysis of the pyrolysis effects on oil shale pore structures at multiscale using different measurement methods. Energy 227, 120359. https://doi.org/10.1016/j.energy.2021.120359.
Li, A., Ding, W.L., Jiu, K., et al., 2018. Investigation of the pore structures and fractal characteristics of marine shale reservoirs using NMR experiments and image analyses: A case study of the Lower Cambrian Niutitang Formation in northern Guizhou Province, South China. Mar. Petrol. Geol. 89, 530–540. https://doi.org/10.1016/j.marpetgeo.2017.10.019.
Li, B., Chen, F.W., Xiao, D.S., et al., 2019. Effect of particle size on the experiment of low temperature nitrogen adsorption: A case study of marine gas shale in Wufeng–Longmaxi Formation. J. China Univ. Min. Technol. 48 (2), 395–404. https://doi.org/10.13247/j.cnki.jcumt.000931 (in Chinese).
Li, W.Q., Cao, J.R., Liang, Y.F., et al., 2024. Evaluation of CO_2 storage and enhanced gas recovery potential in gas shale using kerogen nanopore systems with

mesopores and micropores. Chem. Eng. J. 486, 150225. https://doi.org/10.1016/j.cej.2024.150225.
Li, Z., Jiang, Z.X., Tang, X.L., et al., 2017. Lithofacies characteristics and its effect on pore structure of the marine shale in the low Silurian Longmaxi Formation, southeastern Chongqing. Earth Sci. 42 (7), 1116–1123. https://doi.org/10.3799/dqkx.2017.090 (in Chinese).
Liu, B., Mastalerz, M., Schieber, J., 2022. SEM petrography of dispersed organic matter in black shales: A review. Earth Sci. Rev. 224, 103874. https://doi.org/10.1016/j.earscirev.2021.103874.
Liu, B., Mohammadi, M.R., Ma, Z.L., et al., 2023. Pore structure evolution of Qingshankou shale (kerogen type I) during artificial maturation via hydrous and anhydrous pyrolysis: Experimental study and intelligent modeling. Energy 282, 128359. https://doi.org/10.1016/j.energy.2023.128359.
Liu, K.Q., Jin, Z.J., Zakharova, N., et al., 2021. Proper experimental parameters in N_2 adsorption: The effects of data points and equilibrium interval time. Energy Fuels 35 (24), 20060–20070. https://doi.org/10.1021/acs.energyfuels.1c03257.
Liu, K.Q., Ostadhassan, M., 2019. The impact of pore size distribution data presentation format on pore structure interpretation of shales. Adv. Geo-Energy Res. 3 (2), 187–197. https://doi.org/10.26804/ager.2019.02.08.
Löhr, S.C., Baruch, E.T., Hall, P.A., et al., 2015. Is organic pore development in gas shales influenced by the primary porosity and structure of thermally immature organic matter? Org. Geochem. 87, 119–132. https://doi.org/10.1016/j.orggeochem.2015.07.010.
López, C., Wang, D., Naranjo, Á., et al., 2022. Box-cox-sparse-measures-based blind filtering: Understanding the difference between the maximum kurtosis deconvolution and the minimum entropy deconvolution. Mech. Syst. Signal Process. 165, 108376. https://doi.org/10.1016/j.ymssp.2021.108376.
Loucks, R.G., Reed, R.M., Ruppel, S.C., et al., 2009. Morphology, genesis, and distribution of nanometer-scale pores in siliceous mudstones of the Mississippian Barnett Shale. J. Sediment. Res. 79 (12), 848–861. https://doi.org/10.2110/jsr.2009.092.
Loucks, R.G., Reed, R.M., Ruppel, S.C., et al., 2012. Spectrum of pore types and networks in mudrocks and a descriptive classification for matrix-related mudrock pores. AAPG Bull. 96 (6), 1071–1098. https://doi.org/10.1306/08171111061.
Lu, S.F., Li, J.Q., Xiao, D.S., et al., 2022. Research progress of microscopic pore–throat classification and grading evaluation of shale reservoirs: A minireview. Energy Fuel. 36 (9), 4677–4690. https://doi.org/10.1021/acs.energyfuels.2c00431.
Lu, S.F., Li, J.Q., Zhang, P.F., et al., 2018. Classification of microscopic pore-throats and the grading evaluation on shale oil reservoirs. Petrol. Explor. Dev. 45 (3), 452–460. https://doi.org/10.1016/S1876-3804(18)30050-8.
Luffel, D.L., Guidry, F.K., 1992. New core analysis methods for measuring reservoir rock properties of Devonian shale. J. Petrol. Technol. 44 (11), 1184–1190. https://doi.org/10.2118/20571-PA.
Ma, L., Fauchille, A.L., Dowey, P.J., et al., 2017. Correlative multi-scale imaging of shales: A review and future perspectives. Geol. Soc. Lond. Spec. Publ. 454 (1), 175–199. https://doi.org/10.1144/SP454.11.
Ma, Y., Zhong, N.N., Cheng, L.J., et al., 2016. Pore structure of the graptolite-derived OM in the Longmaxi Shale, southeastern Upper Yangtze Region, China. Mar. Petrol. Geol. 72, 1–11. https://doi.org/10.1016/j.marpetgeo.2016.01.009.
Mahamud, M.M., Novo, M.F., 2008. The use of fractal analysis in the textural characterization of coals. Fuel 87 (2), 222–231. https://doi.org/10.1016/j.fuel.2007.04.020.
Mahmoud, A., Gajbhiye, R., Li, J., et al., 2023. Digital rock physics (DRP) workflow to assess reservoir flow characteristics. Arabian J. Geosci. 16 (4), 248. https://doi.org/10.1007/s12517-023-11314-3.
Mastalerz, M., Hampton, L.B., Drobniak, A., et al., 2017. Significance of analytical particle size in low-pressure N_2 and CO_2 adsorption of coal and shale. Int. J. Coal Geol. 178, 122–131. https://doi.org/10.1016/j.coal.2017.05.003.
Mastalerz, M., Schieber, J., 2017. Effect of ion milling on the perceived maturity of shale samples: Implications for organic petrography and SEM analysis. Int. J. Coal Geol. 183, 110–119. https://doi.org/10.1016/j.coal.2017.10.010.
Mastalerz, M., Schimmelmann, A., Drobniak, A., et al., 2013. Porosity of Devonian and Mississippian New Albany Shale across a maturation gradient: Insights from organic petrology, gas adsorption, and mercury intrusion. AAPG Bull. 97 (10), 1621–1643. https://doi.org/10.1306/04011312194.
Meng, Q.F., Hao, F., Tian, J.Q., 2021. Origins of non-tectonic fractures in shale. Earth Sci. Rev. 222, 103825. https://doi.org/10.1016/j.earscirev.2021.103825.
Milliken, K.L., Curtis, M.E., 2016. Imaging pores in sedimentary rocks: Foundation of porosity prediction. Mar. Petrol. Geol. 73, 590–608. https://doi.org/10.1016/j.marpetgeo.2016.03.020.
Milliken, K.L., Reed, R.M., 2010. Multiple causes of diagenetic fabric anisotropy in weakly consolidated mud, Nankai accretionary prism, IODP Expedition 316. J. Struct. Geol. 32 (12), 1887–1898. https://doi.org/10.1016/j.jsg.2010.03.008.
Milliken, K.L., Rudnicki, M., Awwiller, D.N., et al., 2013. Organic matter–hosted pore system, Marcellus Formation (Devonian), Pennsylvania. AAPG Bull. 97 (2), 177–200. https://doi.org/10.1306/07231212048.
Milner, M., McLin, R., Petriello, J., 2010. Imaging texture and porosity in mudstones and shales: Comparison of secondary and ion-milled backscatter SEM methods. In: Canadian Unconventional Resources and International Petroleum Conference. https://doi.org/10.2118/138975-MS.
Neimark, A.V., Lin, Y.Z., Ravikovitch, P.I., et al., 2009. Quenched solid density functional theory and pore size analysis of micro-mesoporous carbons. Carbon 47 (7), 1617–1628. https://doi.org/10.1016/j.carbon.2009.01.050.
Nelson, P.H., 2009. Pore-throat sizes in sandstones, tight sandstones, and shales. AAPG Bull. 93 (3), 329–340. https://doi.org/10.1306/10240808059.
Nishiyama, N., Yokoyama, T., 2017. Permeability of porous media: Role of the critical pore size. J. Geophys. Res. Solid Earth 122 (9), 6955–6971. https://doi.org/10.1002/2016JB013793.
Ougier-Simonin, A., Renard, F., Boehm, C., et al., 2016. Microfracturing and microporosity in shales. Earth Sci. Rev. 162, 198–226. https://doi.org/10.1016/j.earscirev.2016.09.006.
Peng, N.J., He, S., Hao, F., et al., 2017. The pore structure and difference between Wufeng and Longmaxi shales in Pengshui area, southeastern Sichuan. Earth Sci. 42 (7), 1134–1146. https://doi.org/10.3799/dqkx.2017.092 (in Chinese).
Pinkett, J., Westacott, D., 2016. Innovative sidewall pressure coring technology improves reservoir insight in multiple applications. In: SPWLA 57th Annual Logging Symposium, Reykjavik, Iceland, June 2016, paper number: SPWLA-2016-G.
Pyun, S.I., Rhee, C.K., 2004. An investigation of fractal characteristics of mesoporous carbon electrodes with various pore structures. Electrochim. Acta 49 (24), 4171–4180. https://doi.org/10.1016/j.electacta.2004.04.012.
Radlinski, A.P., 2006. Small-angle neutron scattering and the microstructure of rocks. Rev. Mineral. Geochem. 63 (1), 363–397. https://doi.org/10.2138/rmg.2006.63.14.
Radlinski, A.P., Mastalerz, M., Hinde, A.L., et al., 2004. Application of SAXS and SANS in evaluation of porosity, pore size distribution and surface area of coal. Int. J. Coal Geol. 59 (3–4), 245–271. https://doi.org/10.1016/j.coal.2004.03.002.
Ravikovitch, P.I., Neimark, A.V., 2006. Density functional theory model of adsorption on amorphous and microporous silica materials. Langmuir 22 (26), 11171–11179. https://doi.org/10.1021/la0616146.
Ross, D.J.K., Bustin, R.M., 2009. The importance of shale composition and pore structure upon gas storage potential of shale gas reservoirs. Mar. Petrol. Geol. 26 (6), 916–927. https://doi.org/10.1016/j.marpetgeo.2008.06.004.
Rouquerol, J., Avnir, D., Fairbridge, C.W., et al., 1994. Recommendations for the characterization of porous solids (Technical Report). Pure Appl. Chem. 66 (8), 1739–1758. https://doi.org/10.1351/pac199466081739.
Rouquerol, J., Rouquerol, F., 2014. Methodology of gas adsorption. In: Rouquerol, F., Rouquerol, J., Sing, K.S.W., et al. (Eds.), Adsorption by Powders and Porous Solids: Principles, Methodology and Applications. Elsevier, Amsterdam, pp. 57–104. https://doi.org/10.1016/b978-0-08-097035-6.00003-6.
Ruppert, L.F., Sakurovs, R., Blach, T.P., et al., 2013. A USANS/SANS study of the accessibility of pores in the Barnett Shale to methane and water. Energy Fuel. 27 (2), 772–779. https://doi.org/10.1021/ef301859s.
Saif, T., Lin, Q.Y., Butcher, A.R., et al., 2017. Multi-scale multi-dimensional microstructure imaging of oil shale pyrolysis using X-ray micro-tomography, automated ultra-high resolution SEM, MAPS Mineralogy and FIB-SEM. Appl. Energy 202, 628–647. https://doi.org/10.1016/j.apenergy.2017.05.039.
Sanei, H., Ardakani, O.H., 2016. Alteration of organic matter by ion milling. Int. J. Coal Geol. 163, 123–131. https://doi.org/10.1016/j.coal.2016.06.021.
Saraf, S., Bera, A., 2021. A review on pore-scale modeling and CT scan technique to characterize the trapped carbon dioxide in impermeable reservoir rocks during sequestration. Renew. Sustain. Energy Rev. 144, 110986. https://doi.org/10.1016/j.rser.2021.110986.
Schankula, C.W., Anand, C.K., Bassim, N.D., 2018. Multi-angle plasma focused ion beam (FIB) curtaining artifact correction using a Fourier-based linear optimization model. Microsc. Microanal. 24 (6), 657–666. https://doi.org/10.1017/s1431927618015234.
Schmitt, M., Fernandes, C.P., da Cunha Neto, J.A.B., et al., 2013. Characterization of pore systems in seal rocks using Nitrogen Gas Adsorption combined with Mercury Injection Capillary Pressure techniques. Mar. Petrol. Geol. 39 (1), 138–149. https://doi.org/10.1016/j.marpetgeo.2012.09.001.
Shao, D.Y., Zhang, T.W., Li, Y.F., et al., 2022. Effects of confining pressure and microscale heterogeneity on hydrocarbon retention and pore evolution from artificial maturation of Eagle Ford Shale. Int. J. Coal Geol. 260, 104057. https://doi.org/10.1016/j.coal.2022.104057.
Shu, Y., Xu, S., Yang, F., et al., 2020. The role of microfabric and laminae on pore structure and gas transport pathways of marine shales from Sichuan Basin, China. Geofluids, 8844229. https://doi.org/10.1155/2020/8844229.
Silin, D., Kneafsey, T.J., 2012. Shale gas: Nanometer-scale observations and well modelling. J. Can. Petrol. Technol. 51 (6), 464–475. https://doi.org/10.2118/149489-PA.
Slatt, R.M., O'Brien, N.R., 2011. Pore types in the Barnett and Woodford gas shales: Contribution to understanding gas storage and migration pathways in fine-grained rocks. AAPG Bull. 95 (12), 2017–2030. https://doi.org/10.1306/03301110145.
Song, D.J., Wang, X.Q., Wu, C.J., et al., 2021. Petroleum generation, retention, and expulsion in lacustrine shales using an artificial thermal maturation approach: Implications for the in-situ conversion of shale oil. Energy Fuels 35 (1), 358–373. https://doi.org/10.1021/acs.energyfuels.0c03045.
Song, L.S., Warner, T., Carr, T., 2019. An efficient, consistent, and trackable method to quantify organic matter–hosted porosity from ion-milled scanning electron microscope images of mudrock gas reservoirs. AAPG Bull. 103 (6), 1473–1492. https://doi.org/10.1306/12131817231.
Song, Y.Q., Kausik, R., 2019. NMR application in unconventional shale reservoirs–A new porous media research frontier. Prog. Nucl. Magn. Reson. Spectrosc. 112–113, 17–33. https://doi.org/10.1016/j.pnmrs.2019.03.002.
Sulucarnain, I.D., Sondergeld, C.H., Rai, C.S., 2012. An NMR Study of shale wettability and effective surface relaxivity. In: SPE Canadian Unconventional Resources Conference. https://doi.org/10.2118/162236-MS. Calgary, Alberta, Canada, October 2012, paper number: SPE-162236-MS.

Sun, J.M., Dong, X., Wang, J.J., et al., 2016. Measurement of total porosity for gas shales by gas injection porosimetry (GIP) method. Fuel 186, 694–707. https://doi.org/10.1016/j.fuel.2016.09.010.
Sun, M.D., Zhang, L.H., Hu, Q.H., et al., 2020b. Multiscale connectivity characterization of marine shales in southern China by fluid intrusion, small-angle neutron scattering (SANS), and FIB-SEM. Mar. Petrol. Geol. 112, 104101. https://doi.org/10.1016/j.marpetgeo.2019.104101.
Sun, M.D., Zhao, J.L., Pan, Z.J., et al., 2020a. Pore characterization of shales: a review of small angle scattering technique. J. Nat. Gas Sci. Eng. 78, 103294. https://doi.org/10.1016/j.jngse.2020.103294.
Sun, Y., Wang, Y.P., Liao, L.L., et al., 2023. How grain size influences hydrocarbon generation and expulsion of shale based on Rock-Eval pyrolysis and kinetics? Mar. Petrol. Geol. 155, 106369. https://doi.org/10.1016/j.marpetgeo.2023.106369.
Svergun, D.I., 1991. Mathematical methods in small-angle scattering data analysis. J. Appl. Crystallogr. 24 (5), 485–492. https://doi.org/10.1107/s0021889891001280.
Tang, X.L., Jiang, Z.X., Jiang, S., et al., 2016. Effect of organic matter and maturity on pore size distribution and gas storage capacity in high-mature to post-mature shales. Energy Fuels 30 (11), 8985–8996. https://doi.org/10.1021/acs.energyfuels.6b01499.
Thommes, M., Cychosz, K.A., Neimark, A.V., 2012. Advanced physical adsorption characterization of nanoporous carbons. In: Tascón, J.M.D. (Ed.), Novel Carbon Adsorbents. Elsevier, Amsterdam, pp. 107–145. https://doi.org/10.1016/b978-0-08-097744-7.00004-1.
Thommes, M., Kaneko, K., Neimark, A.V., et al., 2015. Physisorption of gases, with special reference to the evaluation of surface area and pore size distribution (IUPAC Technical Report). Pure Appl. Chem. 87 (9–10), 1051–1069. https://doi.org/10.1515/pac-2014-1117.
Tian, H., Pan, L., Xiao, X.M., et al., 2013. A preliminary study on the pore characterization of Lower Silurian black shales in the Chuandong Thrust Fold Belt, southwestern China using low pressure N_2 adsorption and FE-SEM methods. Mar. Petrol. Geol. 48, 8–19. https://doi.org/10.1016/j.marpetgeo.2013.07.008.
Tinni, A., Odusina, E., Sulucarnain, I., et al., 2014b. NMR response of brine, oil, and methane in organic rich shales. In: SPE Unconventional Resources Conference. https://doi.org/10.2118/168971-MS. The Woodlands, Texas, USA, April 2014, paper number: SPE-168971-MS.
Tinni, A., Sondergeld, C., Rai, C., 2014a. Particle size effect on porosity and specific surface area measurements of shales. In: International Symposium of the Society of Core Analysts, Avignon, France, 8–11 September, 2014, paper number: SCA2014-013.
Tomkus, V., Girdauskas, V., Dudutis, J., et al., 2020. Laser wakefield accelerated electron beams and betatron radiation from multijet gas targets. Sci. Rep. 10, 16807. https://doi.org/10.1038/s41598-020-73805-7.
Torabi, A., Fossen, H., Braathen, A., 2013. Insight into petrophysical properties of deformed sandstone reservoirs. AAPG Bull. 97 (4), 619–637. https://doi.org/10.1306/10031212040.
Wang, G.C., Ju, Y.W., Yan, Z.F., et al., 2015a. Pore structure characteristics of coal-bearing shale using fluid invasion methods: a case study in the Huainan–Huaibei Coalfield in China. Mar. Petrol. Geol. 62, 1–13. https://doi.org/10.1016/j.marpetgeo.2015.01.001.
Wang, M., Ma, R., Li, J.B., et al., 2019a. Occurrence mechanism of lacustrine shale oil in the Paleogene Shahejie Formation of Jiyang Depression, Bohai Bay Basin, China. Petrol. Explor. Dev. 46 (4), 833–846. https://doi.org/10.1016/S1876-3804(19)60242-9.
Wang, R.Y., Hu, Z.Q., Dong, L., et al., 2021. Advancement and trends of shale gas reservoir characterization and evaluation. Oil Gas Geol. 42 (1), 54–65 (in Chinese).
Wang, X.Q., Sun, L., Zhu, R.K., et al., 2015b. Application of charging effects in evaluating storage space of tight reservoirs: a case study from Permian Lucaogou Formation in Jimusar sag, Junggar Basin, NW China. Petrol. Explor. Dev. 42 (4), 516–524. https://doi.org/10.1016/S1876-3804(15)30044-6.
Wang, Y., Cheng, H., 2023. Advances in microscopic pore structure characterization of fine-grained mudrocks. Energy Fuels 37 (3), 1495–1510. https://doi.org/10.1021/acs.energyfuels.2c03144.
Wang, Y., Liu, L.F., Zheng, S.S., et al., 2019b. Full-scale pore structure and its controlling factors of the Wufeng–Longmaxi shale, southern Sichuan Basin, China: implications for pore evolution of highly overmature marine shale. J. Nat. Gas Sci. Eng. 67, 134–146. https://doi.org/10.1016/j.jngse.2019.04.020.
Wang, Y., Pu, J., Wang, L.H., et al., 2016. Characterization of typical 3D pore networks of Jiulaodong formation shale using nano-transmission X-ray microscopy. Fuel 170, 84–91. https://doi.org/10.1016/j.fuel.2015.11.086.
Wang, Y.M., Dong, D.Z., Yang, H., et al., 2014. Quantitative characterization of reservoir space in the Lower Silurian Longmaxi Shale, southern Sichuan, China. Sci. China Earth Sci. 57 (2), 313–322. https://doi.org/10.1007/s11430-013-4645-y.
Wang, Y.M., Wang, Z.L., Zhang, Z.C., et al., 2024. Recent techniques on analyses and characterizations of shale gas and oil reservoir. Energy Rev. 3 (2), 100067. https://doi.org/10.1016/j.enrev.2023.100067.
Wei, B., Wang, B.W., Li, X., et al., 2023. CO_2 storage in depleted oil and gas reservoirs: A review. Adv. Geo-Energy Res. 9 (2), 76–93. https://doi.org/10.46690/ager.2023.08.02.
Wei, M.M., Xiong, Y.Q., Zhang, L., et al., 2016. The effect of sample particle size on the determination of pore structure parameters in shales. Int. J. Coal Geol. 163, 177–185. https://doi.org/10.1016/j.coal.2016.07.013.
Wu, S.T., Yang, Z., Pan, S.Q., et al., 2020b. Three-dimensional imaging of fracture propagation in tight sandstones of the Upper Triassic Chang 7 member, Ordos Basin, Northern China. Mar. Petrol. Geol. 120, 104501. https://doi.org/10.1016/j.marpetgeo.2020.104501.
Wu, S.T., Yang, Z., Zhai, X.F., et al., 2019. An experimental study of organic matter, minerals and porosity evolution in shales within high-temperature and high-pressure constraints. Mar. Petrol. Geol. 102, 377–390. https://doi.org/10.1016/j.marpetgeo.2018.12.014.
Wu, Y.Q., Tahmasebi, P., Yu, H., et al., 2020a. Pore-scale 3D dynamic modeling and characterization of shale samples: considering the effects of thermal maturation. J. Geophys. Res. Solid Earth 125. https://doi.org/10.1029/2019JB018309 e2019JB018309.
Wu, Z.B., Sun, Z., Shu, K., et al., 2024. Mechanism of shale oil displacement by CO_2 in nanopores: A molecular dynamics simulation study. Adv. Geo-Energy Res. 11 (2), 141–151. https://doi.org/10.46690/ager.2024.02.06.
Xia, X.Y., Michael, E., Gao, Y.L., 2020. Preservation of lateral pressure disequilibrium during the uplift of shale reservoirs. AAPG Bull. 104 (4), 825–843. https://doi.org/10.1306/0816191615717370.
Xia, Y.X., Cai, J.C., Perfect, E., et al., 2019. Fractal dimension, lacunarity and succolarity analyses on CT images of reservoir rocks for permeability prediction. J. Hydrol. 579, 124198. https://doi.org/10.1016/j.jhydrol.2019.124198.
Xu, S., Gou, Q.Y., Hao, F., et al., 2020a. Shale pore structure characteristics of the high and low productivity wells, Jiaoshiba shale gas field, Sichuan Basin, China: dominated by lithofacies or preservation condition? Mar. Petrol. Geol. 114, 104211. https://doi.org/10.1016/j.marpetgeo.2019.104211.
Xu, S., Gou, Q.Y., Hao, F., et al., 2020b. Multiscale faults and fractures characterization and their effects on shale gas accumulation in the Jiaoshiba area, Sichuan Basin, China. J. Petrol. Sci. Eng. 189, 107026. https://doi.org/10.1016/j.petrol.2020.107026.
Xu, S., Hao, F., Shu, Z.G., et al., 2020c. Pore structures of different types of shales and shale gas exploration of the Ordovician Wufeng and Silurian Longmaxi successions in the eastern Sichuan Basin, South China. J. Asian Earth Sci. 193, 104271. https://doi.org/10.1016/j.jseaes.2020.104271.
Xu, S., Wen, J., Liu, K.Q., et al., 2024. Brittle minerals, mechanical properties and fracability evaluation of shales. Adv. Geo-Energy Res. 14 (1), 8–11. https://doi.org/10.46690/ager.2024.10.03.
Xu, S., Yang, D., Liu, B.C., et al., 2025. Multi-field coupling controls the formation and evolution of deep reservoirs. Adv. Geo-Energy Res. 17 (2), 176–178. https://doi.org/10.46690/ager.2025.08.08.
Yang, R., Hu, Q.H., He, S., et al., 2018. Pore structure, wettability and tracer migration in four leading shale formations in the Middle Yangtze Platform. China. Mar. Petrol. Geol. 89, 415–427. https://doi.org/10.1016/j.marpetgeo.2017.10.010.
Yang, W., Xu, L., Chen, D.X., et al., 2021. How argillaceous reservoirs exhibit better quality than silty mudstones? Anomalous behavior of shale gas-bearing properties of continental fine-grained sediments in Southwest China and its possible forcing mechanisms. Pet. Sci. 18 (6), 1589–1610. https://doi.org/10.1016/j.petsci.2021.09.032.
Yang, W., Xue, L.H., Tang, J., et al., 2015. Analysis and evaluation of different measuring methods for shale porosity. Acta Sedimentol. Sin. 33 (6), 1258–1264. https://doi.org/10.14027/j.cnki.cjxb.2015.06.018 (in Chinese).
Yang, W., Yang, R., Wang, M., et al., 2025. Impact of lithofacies categories on inflection-point behaviors in micro-nano pore-structure evolution: Implications for differential reservoir-forming mechanisms and “sweet-spot intervals” identification for marine gas shales. Mar. Petrol. Geol. 176, 107336. https://doi.org/10.1016/j.marpetgeo.2025.107336.
Yao, Y.B., Liu, D.M., 2018. Petrophysical properties and fluids transportation in gas shale: A NMR relaxation spectrum analysis method. J. China Coal Soc. 43 (1), 181–189 (in Chinese). https://doi.org/10.13225/j.cnki.jccs.2017.4002.
Yao, Y.B., Liu, D.M., Tang, D.Z., et al., 2008. Fractal characterization of adsorption-pores of coals from North China: An investigation on CH_4 adsorption capacity of coals. Int. J. Coal Geol. 73 (1), 27–42. https://doi.org/10.1016/j.coal.2007.07.003.
Yu, B.S., 2013. Classification and characterization of gas shale system. Earth Sci. Front. 20 (4), 211–220 (in Chinese).
Yu, H., Fan, J.C., Xia, J., et al., 2020. Multiscale gas transport behavior in heterogeneous shale matrix consisting of organic and inorganic nanopores. J. Nat. Gas Sci. Eng. 75, 103139. https://doi.org/10.1016/j.jngse.2019.103139.
Yu, W., Sepehrnoori, K., 2014. An efficient reservoir-simulation approach to design and optimize unconventional gas production. J. Can. Petrol. Technol. 53 (2), 109–121. https://doi.org/10.2118/165343-PA.
Zhang, C., Shan, W., Wang, X., 2019. Quantitative evaluation of organic porosity and inorganic porosity in shale gas reservoirs using logging data. Energy Sources Part A recovery util. Environ. Eff. 41 (7), 811–828. https://doi.org/10.1080/15567036.2018.1520361.
Zhang, P.F., Lu, S.F., Li, J.Q., 2018a. Petrophysical characterization of oil-bearing shales by low-field nuclear magnetic resonance (NMR). Mar. Petrol. Geol. 89, 775–785. https://doi.org/10.1016/j.marpetgeo.2017.11.015.
Zhang, J.Z., Tang, Y.J., He, D.X., et al., 2020. Full-scale nanopore system and fractal characteristics of clay-rich lacustrine shale combining FE-SEM, nano-CT, gas adsorption and mercury intrusion porosimetry. Appl. Clay Sci. 196, 105758. https://doi.org/10.1016/j.clay.2020.105758.
Zhang, Q.G., Huang, Y.S., Zhang, R.J., et al., 2021. Study on porosity interpretation model of shale oil reservoir based on geochemical parameters. Unconv. Oil Gas 8 (5), 9–18. https://doi.org/10.19901/j.fcgyq.2021.05.02 (in Chinese).
Zhang, S.W., Xian, X.F., Zhou, J.P., et al., 2018b. Experimental study of the pore structure characterization in shale with different particle size. J. Energy Resour. Technol. 140 (5), 054502. https://doi.org/10.1115/1.4039022.
Zhao, J.H., Hu, Q.H., Liu, K.Y., et al., 2020. Pore connectivity characterization of shale using integrated wood’s metal impregnation, microscopy, tomography, tracer mapping and porosimetry. Fuel 259, 116248. https://doi.org/10.1016/j.fuel.2019.116248.
Zhao, L.X., Zhu, J.W., Qin, X., et al., 2023a. Joint geochemistry-rock physics modeling: quantifying the effects of thermal maturity on the elastic and

anisotropic properties of organic shale. Earth Sci. Rev. 247, 104627. https://doi.org/10.1016/j.earscirev.2023.104627.
Zhao, R.X., Lu, S.F., Xue, H.T., et al., 2019. Effect of SEM parameters on quantitative evaluation of shale micropores. Oil Gas Geol. 40 (5), 1141–1154. https://doi.org/10.11743/ogg20190520 (in Chinese).
Zhao, R.X., Xue, H.T., Lu, S.F., et al., 2022. Multi-scale pore structure characterization of lacustrine shale and its coupling relationship with material composition: An integrated study of multiple experiments. Mar. Petrol. Geol. 140. https://doi.org/10.1016/j.marpetgeo.2022.105648.
Zhao, S., Lu, S.F., Wu, J.F., et al., 2023b. Comparison and verification of gas-bearing parameter evaluation methods for deep shale based on the pressure coring technique. Energy Fuel. 37 (3), 2066–2077. https://doi.org/10.1021/acs.energyfuels.2c03840.
Zhou, S.D., Pan, Z.J., Yan, D.T., et al., 2024a. Geochemical and petrophysical characterization of potential gas shale reservoirs in the Lishu depression, southern Songliao Basin, northeastern China. AAPG Bull. 108 (9), 1799–1826. https://doi.org/10.1306/05212420161.
Zhou, S.W., Dong, D.Z., Zhang, J.H., et al., 2021. Optimization of key parameters for porosity measurement of shale gas reservoirs. Nat. Gas Ind. B 8 (5), 455–463. https://doi.org/10.1016/j.ngib.2021.08.004.
Zhou, Y., Guan, W., Zhao, C.M., et al., 2024b. Numerical methods to simulate spontaneous imbibition in microscopic pore structures: a review. Capillarity 11 (1), 1–21. https://doi.org/10.46690/capi.2024.04.01.
Zhu, H.J., Huang, C., Ju, Y.W., et al., 2021. Multi-scale multi-dimensional characterization of clay-hosted pore networks of shale using FIBSEM, TEM, and X-ray micro-tomography: Implications for methane storage and migration. Appl. Clay Sci. 213, 106239. https://doi.org/10.1016/j.clay.2021.106239.
Zhu, R.K., Wu, S.T., Cui, J.W., et al., 2016. Classification and evaluation of pore size in oil & gas reservoir rocks. Geol. Sci. Technol. Inf. 35 (3), 133–144 (in Chinese).
Zou, C.N., Yang, Z., Zhang, G.S., et al., 2023. Theory, technology and practice of unconventional petroleum geology. J. Earth Sci. 34 (4), 951–965. https://doi.org/10.1007/s12583-023-2000-8.
Zou, C.N., Zhu, R.K., Bai, B., et al., 2011. First discovery of nano-pore throat in oil and gas reservoir in China and its scientific value. Acta Pet. Sin. 27 (6), 1857–1864 (in Chinese).
Zou, S.M., Sun, C.H., 2020. X-ray microcomputed imaging of wettability characterization for multiphase flow in porous media: A review. Capillarity 3 (3), 36–44. https://doi.org/10.46690/capi.2020.03.01.